

AMBIENT NOISE FROM TURBIDITY CURRENTS IN HOWE SOUND

by

Matthew G. Hatcher

Submitted in partial fulfillment of the requirements  
for the degree of Master of Science

at

Dalhousie University  
Halifax, Nova Scotia  
June 2017

© Copyright by Matthew G. Hatcher, 2017

*For Wes*

# TABLE OF CONTENTS

<b>List of Tables</b> . . . . .	<b>vi</b>
<b>List of Figures</b> . . . . .	<b>vii</b>
<b>Abstract</b> . . . . .	<b>ix</b>
<b>List of Abbreviations and Symbols Used</b> . . . . .	<b>x</b>
<b>Acknowledgements</b> . . . . .	<b>xiii</b>
<b>Chapter 1 Introduction</b> . . . . .	<b>1</b>
1.1 Turbidity Currents . . . . .	2
1.2 Sediment-Generated Noise . . . . .	3
1.3 Howe Sound . . . . .	3
1.4 Thesis Goals and Outline . . . . .	4
<b>Chapter 2 Howe Sound Field Experiment</b> . . . . .	<b>6</b>
2.1 Field Experiment and Site . . . . .	6
2.2 Data Sources . . . . .	9
2.2.1 Hydrophone . . . . .	9
2.2.2 M3 Multi-Beam Sonars . . . . .	11
2.2.3 Knudsen Single-Beam Sounders and Kongsberg EM710 Multi- beam sonar . . . . .	12
2.2.4 Acoustic Doppler Current Profiler . . . . .	12
2.2.5 Grab Sample and Sediment Grain Size . . . . .	13
2.2.6 Sound Speed Measurements . . . . .	14
<b>Chapter 3 Theory</b> . . . . .	<b>15</b>
3.1 Turbidity Currents . . . . .	15

3.1.1	Froude Number . . . . .	17
3.1.2	Sediment Size Distribution within Turbidity Currents . . . . .	18
3.1.3	Bedload . . . . .	19
3.2	Sediment Generated Noise (SGN) . . . . .	20
3.2.1	Predicted Spectrum for Idealized Two-Particle Collisions . . . . .	21
3.2.2	Particle Collision Frequency . . . . .	23
3.3	Bubble Noise . . . . .	25
3.4	Sound Propagation Effects . . . . .	26
3.4.1	Ray Tracing Model . . . . .	26
3.4.2	Attenuation . . . . .	27
3.4.3	Hydrophone Listening Radius . . . . .	28
3.4.4	Inferring Sediment Concentration from Backscatter Intensity at Multiple Frequencies . . . . .	29
<b>Chapter 4</b>	<b>Turbidity Current Properties . . . . .</b>	<b>31</b>
4.1	Overview . . . . .	31
4.2	Bubble Sizes . . . . .	33
4.3	Head Properties . . . . .	34
4.4	Body and Tail Properties . . . . .	39
4.5	Suspended Sediment Concentration from Acoustic Backscatter . . . . .	43
<b>Chapter 5</b>	<b>Measured and Predicted Noise from Turbidity Currents . . . . .</b>	<b>46</b>
5.1	Observations . . . . .	46
5.1.1	Event Detection . . . . .	46
5.1.2	The Louder Events . . . . .	48
5.1.3	Turbidity Current Noise Spectra . . . . .	50
5.1.4	Sound Intensity vs. Head Speed . . . . .	50
5.2	Propagation Effects . . . . .	52
5.2.1	Turbidity Current SGN Asymmetry . . . . .	52

5.2.2	2-D Ray Tracing Model . . . . .	53
5.2.3	Hydrophone Listening Radius . . . . .	54
5.2.4	Time Dependence of Sound Emitting Patch . . . . .	55
5.3	Comparison to Theory . . . . .	56
5.3.1	Predicted SGN Spectra . . . . .	57
5.4	Discussion . . . . .	60
5.4.1	Less Intense Events . . . . .	60
5.4.2	Bubble Generated Noise . . . . .	60
5.4.3	Remote Events and Frequency of Occurrence . . . . .	62
5.4.4	SGN: Comparing Predictions and Observations . . . . .	64
<b>Chapter 6</b>	<b>Summary and Conclusions . . . . .</b>	<b>65</b>
<b>Appendix A</b>	<b>. . . . .</b>	<b>68</b>
<b>Appendix B</b>	<b>. . . . .</b>	<b>71</b>
<b>Bibliography</b>	<b>. . . . .</b>	<b>72</b>

# LIST OF TABLES

Table 2.1	Active acoustic instruments . . . . .	12
Table 4.1	Turbidity current properties . . . . .	39
Table 5.1	Turbidity current bedload layer properties . . . . .	58

# LIST OF FIGURES

Figure 2.1	Bathymetry of Squamish delta . . . . .	7
Figure 2.2	Diagram of vessel mooring and instrument frame . . . . .	9
Figure 2.3	Example of active sonar noise removal from hydrophone spectral data	11
Figure 2.4	Grain size distribution . . . . .	13
Figure 3.1	Anatomy of a turbidity current . . . . .	17
Figure 3.2	Diagram of a collision for which the SGN is analytically solvable .	22
Figure 3.3	Sound spectra from simple collisions . . . . .	23
Figure 3.4	Diagram of the collision volume for a moving particle . . . . .	24
Figure 3.5	Diagram of the hydrophone listening radius . . . . .	29
Figure 4.1	Knudsen single-beam sounder backscatter data . . . . .	32
Figure 4.2	EM710 vessel-bottom mounted multibeam backscatter . . . . .	33
Figure 4.3	Bubble rise rates and diameters . . . . .	34
Figure 4.4	Forward-looking M3 multibeam sonar imagery . . . . .	35
Figure 4.5	Head speed of turbidity current 172C estimated from the M3 sounder	36
Figure 4.6	Downward-looking M3 sonar backscatter and turbidity current thickness for event 172C . . . . .	37
Figure 4.7	Shadowgraphs of laboratory saline gravity currents by <i>Britter and Linden</i> (1980) . . . . .	38
Figure 4.8	ADCP velocities, event 172C . . . . .	40
Figure 4.9	ADCP attitude, event 172C . . . . .	41
Figure 4.10	ADCP velocities at 1 m above the bottom, event 172C . . . . .	42
Figure 4.11	Turbidity current thickness and suspended sediment concentration, event 172C . . . . .	43
Figure 4.12	Acoustic backscatter at two frequencies and $\chi$ , event 172C . . . .	44
Figure 4.13	Two frequency inversion for concentration and the slope of $\chi$ , event 172C . . . . .	45

Figure 4.14	Values of $n(\Sigma_{T_1} - \Sigma_{T_2})$ as a function of frequency and suspended sediment concentration . . . . .	45
Figure 5.1	Turbidity current 172C SGN and acoustic backscatter . . . . .	47
Figure 5.2	Ambient noise spectrogram for YD 172 . . . . .	48
Figure 5.3	Spectrograms of louder turbidity current event noise . . . . .	49
Figure 5.4	Turbidity current noise spectra for the louder events . . . . .	50
Figure 5.5	Sound pressure squared as a function of head speed . . . . .	51
Figure 5.6	Temporal asymmetry of the observed noise signal from event 172C	52
Figure 5.7	Sound speed profiles . . . . .	53
Figure 5.8	BELLHOP modelled transmission loss . . . . .	54
Figure 5.9	Listening radius of the hydrophone at 200 kHz as a function of suspended sediment concentration . . . . .	55
Figure 5.10	Predicted and observed onset of noise preceding event 172C . . . . .	56
Figure 5.11	Predicted and observed noise spectra for event 172C . . . . .	59
Figure 5.12	Resonance frequency of bubbles as a function of diameter . . . . .	61
Figure 5.13	Ambient noise spectrogram for distant events . . . . .	62
Figure 5.14	Predicted attenuation of turbidity current noise from a distant source	63

# ABSTRACT

Turbidity currents are gravity currents that derive their density difference from sediment suspended within the fluid. In the marine environment they are responsible for sediment transport on large scales (e.g. it is thought that the bulk of terrigenous mobile sediments in the ocean were carried to abyssal depths by turbidity currents, through geologic time) and smaller scales, such as river deltas. Previous research has shown that sediment being transported in a fluid can produce sediment self-generated noise (SGN), arising from inter-particle collisions within the flow, or the associated bedload transport. Generally turbidity currents are difficult to measure *in situ*, due to their unpredictability in time and space; however, environments where sediment-laden rivers enter fjords, forming deltas, can be an exception. The spatial uncertainty is drastically reduced due to the topographical constraints, and the temporal uncertainty may also be reduced, depending on the trigger mechanism. During a 5 day period in June 2013, measurements were made of turbidity currents in Howe Sound, using both active and passive acoustic instrumentation.

The primary goal of this thesis is to explore the use of passive acoustics for turbidity current detection and monitoring, and further—from the spectral characteristics of turbidity current noise—to establish the likely sound generation mechanism. The spectral shape of the measured turbidity current noise, and that predicted by the SGN mechanism are consistent, indicating turbidity current noise is generated by particle collisions.

The secondary goal is to establish a relationship between the noise signal, and the dynamical properties of these sediment-laden flows. The relationship  $P^2 \propto U_0^7$ , between sound pressure squared—normalized by turbidity current width—and head speed, is consistent with both the measurements and predictions. The predictions use the linear relationship between sound pressure and collision speed (for a single collision), and estimates of rates of collision occurrence, between moving particles, based on the kinetic theory of gases.

# LIST OF ABBREVIATIONS AND SYMBOLS USED

Roman symbol	Description	Units
$(x, y, z)$	cartesian coordinates	m
$(u, v, w)$	velocities in the cartesian coordinate system	$\text{m s}^{-1}$
$(r, \theta, z)$	cylindrical coordinates	(m, °, m)
$F$	Fourier transform operator	
$g$	acceleration due to gravity	$\text{m s}^{-2}$
$g'$	reduced acceleration due to gravity	$\text{m s}^{-2}$
$C_d$	coefficient of drag	
$h$	body thickness of the turbidity current	m
$h_0$	head height of the turbidity current	m
$U$	speed of the body of the turbidity current	$\text{m s}^{-1}$
$U_0$	head speed of the turbidity current	$\text{m s}^{-1}$
$U_c$	particle collision speed	$\text{m s}^{-1}$
$H$	water depth	m
$A_{fr}$	Froude number of the turbidity current using $h_0$	
Fr	Froude number of the turbidity current using $h$	
$u_*$	friction velocity	$\text{m s}^{-1}$
$Q$	volume flux	$\text{m}^3 \text{s}^{-1}$
$w_s$	particle settling velocity	$\text{m s}^{-1}$
$p$	pressure	Pa
$A$	acceleration time history for a particle in a collision	$\text{m s}^{-2}$
$P_i$	impulse response pressure for a sphere	Pa
$f_t$	characteristic frequency associated with a particle collision	$\text{s}^{-1}$
$t_0$	contact time for a particle collision	s
$E$	Young's modulus	$\text{kg m}^{-1} \text{s}^{-2}$
$a$	particle radius	m
$d$	particle diameter	m
$a_b$	bubble radius	m

Roman symbol	Description	Units
$p_h$	hydrostatic pressure	Pa
$r_p$	distance from a collision for the peak pressure calculation	m
$c$	sound speed in water	$\text{m s}^{-1}$
$c_a$	sound speed in air	$\text{m s}^{-1}$
$Z_w$	acoustic impedance in water	$\text{Pa s m}^{-3}$
$Z_a$	acoustic impedance in air	$\text{Pa s m}^{-3}$
$n$	number density of particles	$\text{m}^{-3}$
$n_s$	number of size classes of particles	
$W$	collision rate per unit volume	$\text{m}^{-3} \text{s}^{-1}$
$L_B$	stationary bedload layer thickness	m
$C_v$	volume concentration	
$C_{vb}$	reference volume concentration for the Vanoni distribution	
$b$	reference height for Vanoni distribution	m
$C_{vmax}$	maximum volume concentration when particles are at rest	
$C_{vbl}$	volume concentration in the bedload layer	
$z_{bl}$	mobile bedload layer thickness	m
$z_s$	suspended sediment layer thickness	m
$z_h$	height of receiver above the bed	m
$r_0$	field point distance from a particle collision in the bedload layer	m
$P_0$	source sound pressure per unit area above the bedload layer	m
$z_0$	reference height for $P_0$ above the bedload layer	m
$f_b$	Minnaert resonance frequency	$\text{s}^{-1}$
$(r_s, z_s)$	source location of a beam	m
$I$	sound intensity	$\text{W m}^{-2}$
$I_b$	backscatter intensity	$\text{W m}^{-2}$
$k$	wavenumber	$\text{m}^{-1}$
$K_{TR}$	effective transceiver sensitivity	$\text{W m}$
$R$	slant range	m

Greek symbol	Description	Units
$\Theta$	delta slope	$^\circ$
$\rho$	density of water	$\text{kg m}^{-3}$

Greek symbol	Description	Units
$\rho_t$	density of water with suspended particles in the turbidity current	$\text{kg m}^{-3}$
$\rho_s$	density of sediment particles	$\text{kg m}^{-3}$
$\tau$	local stress	$\text{kg m}^{-1} \text{s}^{-2}$
$\tau_b$	bottom stress	$\text{kg m}^{-1} \text{s}^{-2}$
$\kappa$	von Kármán's constant	
$\nu$	Poisson's ratio	
$\theta_s$	Shields parameter	
$\theta_{sc}$	critical Shields parameter	
$\gamma$	specific heat ratio	
$\Phi$	beam take-off angle	°
$\alpha$	sound attenuation coefficient	$\text{m}^{-1}$
$\alpha_w$	sound attenuation coefficient for water	$\text{m}^{-1}$
$\alpha_s$	sound attenuation coefficient for suspended sediment	$\text{m}^{-1}$
$\lambda$	wavelength	m
$\Sigma_T$	total cross-section	$\text{m}^2$
$\sigma$	specific gravity of the particle material	
$\sigma_b$	back-scattering cross-section	$\text{m}^2$
$\mu$	viscosity	$\text{kg m}^{-1} \text{s}^{-1}$
$\eta$	kinematic viscosity	$\text{m}^2 \text{s}^{-1}$
$\phi$	slant angle	°
$\chi$	Equation 3.36	

# ACKNOWLEDGEMENTS

I would like to thank my supervisor, Dr. Alex Hay, not only for the thorough academic support, but for the financial support to complete this research and thesis. The money was always made available, with no thought or stress on my part, even though there was no specific funding source associated with my work.

Without the field experiment there would be no thesis, and so I am very grateful that Dr. Joun Hughes-Clarke, and the other members of the Ocean Mapping Group (Dr. Danar Pratomo and Dr. Anand Hiroji), made room for me aboard the small survey launch CSL Heron.

All the members of my committee: Dr. David Barclay, Dr. Paul Hines, Dr. John Hughes Clarke and Dr. Barry Ruddick, as well as my external examiner, Dr. Len Zedel, were instrumental in helping me pull this work together, and I am grateful for their support and advice.

This thesis, like most undertakings in life, could not be achieved as an insolated endeavour. It's completion required many educational building blocks extending back before my formal education. My parents, Dr. Bruce G. Hatcher and Dr. Annamarie I. Hatcher, were always educating me and encouraging me to educate myself, both formally and non, and in so doing deserve my gratitude for enabling and encouraging me to complete this thesis.

Last, but emphatically not least, I would like to thank my wife, Katie Arbuckle. While I pursued the enviable, often selfish, task of completing a graduate thesis, she had to pick up more than her fair share of the slack in our shared lives. I love her, and I thank her for this.

---

# CHAPTER 1

---

## INTRODUCTION

The means by which relatively small mobile solids are suspended, moved, and deposited by the dynamics of the fluids in which they exist has long been important to humans, and to life in general. This means of driving morphological change is illustrated by numerous examples on earth, some of which include: the vast dune-fields in the deserts; avalanches on snowy mountains; the sand bars and ripples seen on beaches; and the majority of sea-floor canyons on the continental slopes, and their associated submarine fans in the abyssal ocean. Coastal regions, where the majority of humans live, are often predominately made up of mobile material, and the sea-floor is almost exclusively made up of mobile material. As humans continue to expand their presence and infrastructure on the coasts and adjacent sea-floor, improved knowledge of the fluid dynamics and material transport in these areas is more eagerly sought. The specific mechanisms by which fluids re-work and re-distribute mobile materials are varied, and often complex. For these reasons, a complete physical understanding of most of these mechanisms is lacking, and often so are the observations needed to facilitate this physical understanding.

This thesis focusses on one of these mechanisms that occurs on, and impacts, sea-floors—turbidity currents. The aim is two-fold: to present new and novel *in situ* observations of these currents—which are rare—and to quantify what can be learned about them, and the associated sediment transport, from these observations. Primarily, the feasibility of monitoring and quantifying these currents, and the associated sediment transport, by means of passive acoustics is investigated.

## 1.1 Turbidity Currents

Turbidity currents are a type of gravity current, for which buoyancy is the motive force. They can occur whenever two fluids of different density exist and are not arranged in a stable gravitational state; that is, the gravitational potential energy of the system is not minimized. In the ocean there can be many causes of density differences between parcels of fluid, for instance temperature and salinity. However, turbidity currents derive their density difference from suspended sediment within the current. Similarly, there are many reasons why a fluid of greater density would find itself above one of lesser. In the case of turbidity currents this generally only happens in the vicinity of sloping bottoms. Some trigger is required for initial suspension of the particles, at some point on the slope, and, if conditions are favourable a flow will develop on the slope, which can attain enough momentum to travel appreciable distances onto the flat area beyond.

Turbidity currents are immensely important in creating, and altering, sea-floor morphology. These discrete events are thought to have created the majority of the continental slope submarine canyons, and carried the bulk of terrigenous sediments from the continental shelves out onto the abyssal plains (e.g. *Daly (1936)*). More generally, they are the dominant mechanism for transport of sediments to greater depths elsewhere in the ocean, including inner shelf environments during storms (e.g. *Xu et al. (2004)*), and delta fronts (e.g. *Prior et al. (1987)*; *Bornhold et al. (1994)*; *Hughes Clarke et al. (2012)*; *Hughes Clarke (2016)*). They also have the potential to become very energetic and to destroy infrastructure in their path, such as submarine cables (e.g. *Heezen and Ewing (1952)*).

Direct observations of turbidity currents *in situ* exist (e.g. *Hay (1987)*; *Prior et al. (1987)*; *Zeng et al. (1991)*; *Bornhold et al. (1994)*; *Xu et al. (2004)*; *Hughes Clarke et al. (2012)*; *Hughes Clarke (2016)*) but are rare. This is mainly due to the fact that they are usually unpredictable in both space and time, due to their discrete nature, and the need for a triggering mechanism. Large scale events are often triggered by seismic activity, and smaller scale events are common at river mouths, where sediment laden water encounters a delta slope. These factors make this important transport mechanism very hard to observe and quantify *in situ*.

## 1.2 Sediment-Generated Noise

The collision between two solids within a fluid can create a compressional pressure wave (sound) within that fluid. Recently work has been done (*Bedeus and Ivicsics* (1963); *Johnson and Muir* (1969); *Tywoniuk and Warnock* (1973); *Jonys* (1976); *Richards and Milne* (1979), *Thorne et al.* (1984); *Williams et al.* (1989); *Mason et al.* (2007); *Barton et al.* (2010); *Camenen et al.* (2012) and *Bassett et al.* (2013) among others) to make use of this phenomenon as it relates to sediment movement in water. Analytical solutions to simplified problems involving two spheres colliding in a fluid were first pursued by those predominately interested in machine noise in air (*Banerji* (1916); *Banerji* (1918); *Koss and Alfredson* (1973); *Koss* (1974a); *Koss* (1974b); *Akay and Hodgson* (1978a); *Akay and Hodgson* (1978b); *Akay* (1978) among others). These ideas have been adapted by *Thorne* (1985,1986) to describe the sound-field produced by multiple random collisions between natural sand- and gravel-sized particles in water. This sound-field has been termed sediment self-generated noise, shortened here to sediment-generated noise (SGN). *Thorne* (1986) has shown that for the case of solid particles (of similar composition and size to naturally occurring sediments) colliding in water, the dominant mechanism of sound production is rigid body radiation. Sound is predominately due to the acceleration and deceleration of the rigid particles, and the associated compression and rarefaction this produces in the fluid, as opposed to collision-induced resonances within the particles. This knowledge has motivated efforts to quantify sediment transport using passive acoustic measurements of sound radiated from particle collisions, during active transport conditions (e.g. *Thorne et al.* (1984), *Williams et al.* (1989), and *Voulgaris et al.* (1995)).

## 1.3 Howe Sound

Howe Sound is a 280 m deep fjord with a shallow river-delta at the head, and a number of islands and channels opening up to the Strait of Georgia at the mouth. The delta is continually fed with fresh, sediment-laden water from the Squamish River. The river is glacially fed from the British Columbia Coast Range mountains, and experiences the spring freshet associated with spring-time snow melt. The fjord bottom and delta are made up of the sediments delivered by the river, fine sand. The depth on the delta slope falls off from less than 1 m at the delta lip, to greater than 100 m within 1 km. The sea floor

morphology is characterized by channels incised in the delta slope and out into the fjord. The presence of well defined cyclic steps on the bottom of these channels indicates that fast, super-critical, turbidity currents flow down them relatively frequently (*Hughes Clarke et al. (2012), Hughes Clarke (2016)*).

## 1.4 Thesis Goals and Outline

The goals of this thesis are: (i) to present what appears to be the first passive acoustic measurements of turbidity currents in the field, and to determine whether particle collisions associated with the currents is the mechanism of sound generation (i.e. SGN), and (ii) to relate the properties of the recorded acoustic signal to the flow, and sediment transport, conditions within the turbidity current. To achieve these goals, five main questions are posed:

- 1) Can we detect turbidity currents using passive acoustic monitoring? That is, is it feasible to monitor the occurrence of turbidity currents using the noise they generate?
- 2) Is the measured acoustic signal from the turbidity currents caused by sediment motion associated with the turbidity current? Specifically, is the signal's spectral shape consistent with previous results and theory about SGN? Or, is another mechanism responsible for sound production in the Howe Sound data?
- 3) Is the magnitude of the measured spectrum consistent with the SGN theory? Specifically, is the magnitude of the spectrum consistent with independently estimated concentrations of mobile material, collision speeds, and the frequency of collisions between the particles involved in the SGN mechanism?
- 4) The acoustic backscatter measurements show evidence of bubbles being released from the seabed during some turbidity currents. What is the contribution of these bubbles to the spectrum of the measured noise signal?
- 5) The noise spectra associated with the most intense measured turbidity currents exhibit a temporal asymmetry, characterized by an abrupt increase in noise, followed by a peak, and then a gradual falloff. What is the cause of this temporal asymmetry?
- 6) What is the relationship between the sound intensity and the dynamics of the turbidity current? Can a relationship between turbidity current sound intensity and head speed be inferred?

These questions are investigated in the context of the multi-instrument Howe Sound

field dataset, and a model of turbidity current SGN production. The model is based on the analytical solution derived by *Thorne and Foden* (1988) for the sound spectrum produced by a head-on, two-particle elastic collision, and a collision frequency, following that in the classical kinetic theory of gases (e.g. *McNaught and Wilkinson* (1997)).

The thesis is organised as follows. Chapter 2 contains an overview of the field site, the experiment, and the types and methods of data collection and processing. Chapter 3 outlines the necessary theory, including: (a) the (semi-empirical) theory governing turbidity current flow speeds and sediment concentrations; (b) noise generation by particle collisions; and (c) sound propagation through sediment suspensions and seawater, including attenuation and refraction. Chapter 4 presents measured and inferred properties of the turbidity currents observed in the field experiment. Primarily, turbidity current properties relevant to predicted sound pressure (e.g. characteristic flow speeds and sediment concentrations) are presented. In Chapter 5 measurements of turbidity current noise are presented, and are related to independent measurements of turbidity current properties; primarily, turbidity current head speed. Further, theoretically predicted spectral sound pressure levels are compared to the field measurements. Chapter 6 concludes and summarises the thesis, and suggests future work.

---

## CHAPTER 2

---

# HOWE SOUND FIELD EXPERIMENT

In June 2013 a field experiment was carried out in Howe Sound, on the Squamish River delta. Prior field experiments monitoring the morphological change of the river delta indicated that turbidity currents frequently occurred there (*Hughes Clarke et al. (2012)*), which prompted an effort to monitor and measure them *in situ*. In 2013, in addition to monitoring the delta for morphological change, many instruments were deployed with the aim of providing these *in situ* measurements (*Hughes Clarke (2016)*). The majority of these were active acoustic instruments intended to provide sonar imagery and current velocities. However, this thesis focuses on passive acoustic measurements made by an omni-directional hydrophone, mounted on a frame suspended roughly 10 m above the bottom. The active acoustic instruments mounted to this frame, as well as the research vessel, provided independent measurements of the turbidity currents, used to confirm and compliment the passive acoustic measurements.

### 2.1 Field Experiment and Site

Howe Sound is characterized by a 280 m deep Fjord with a shallow river-delta at the head, and a number of islands and channels opening into the Strait of Georgia at the mouth (Figure 2.1). The delta is continually fed with fresh, sediment-laden water from the Squamish river. The bottom in the vicinity of the delta is made up of a broad, uni-modal, fine sand. The delta top is the shallow, flat topography in the area where the river enters the fjord, at the delta lip the depth falls off steeply from less than 1 m to greater than 100 m within 1 km, down-Fjord from the lip. This sloping bottom is the delta slope. The sea floor morphology is dominated by channels incised in the delta slope and out into the fjord.

Well defined cyclic steps are present on the bottom of these channels, and are formed by turbidity currents with supercritical Froude numbers (*Hughes Clarke et al. (2012)*, *Hughes Clarke (2016)*). Similar bedforms outside the channels are likely remnant features due to the dynamic nature of bedload transport in the area, i.e. channels either move laterally, or are replaced by new channels with different source points, over time. Previous studies at the site have shown that turbidity currents occur relatively regularly on the delta slope. The frequency of occurrence increases during times of higher river discharge and lower low water during spring tides (*Hughes Clarke et al. (2012)*).

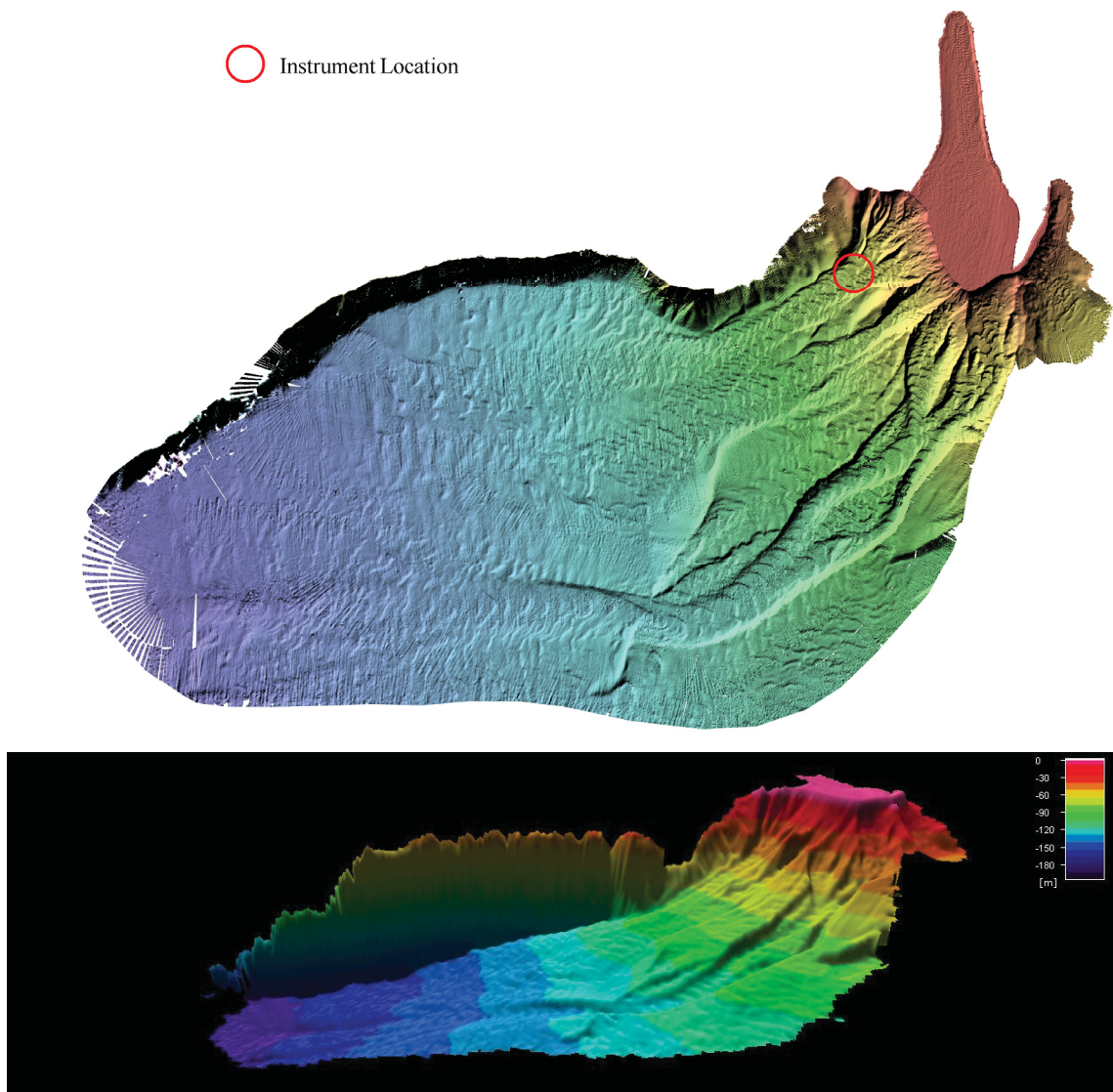


Figure 2.1: Bathymetry of Squamish delta. Location of moored vessel denoted by red circle (Courtesy of Danar Pratomo, UNB).

During the days June 18-22, 2013 the survey vessel *Heron*, operated by the University of New Brunswick (UNB) Ocean Mapping Group, was moored at N 49.68117, W 123.18447 (Figure 2.1). The goal was to obtain real-time *in situ* measurements of turbidity currents in the channel beneath, flowing past the mooring location. Specifically, the hydrophone was deployed with the aim of measuring sound generated by turbidity currents, at as minimum a distance as possible, while still remaining outside the area of fluid flow associated with the turbidity currents. The position of the vessel was maintained through the use of a four-point mooring system. *Heron* would tie up to the floats for roughly four hours each day coinciding with the lower low tide. An instrument frame was lowered over the side and held, suspended approximately 10 m above the bottom (Figure 2.2). Mounted on the frame were an Ocean Sonics, icListen HF omnidirectional hydrophone and two Kongsberg Mesotech M3 multibeam sonar's—one directed horizontally, and the other downward. Fore-and-aft lowering/support lines were used to control the frame attitude. This was made possible by relatively quiescent conditions at depth, and the fact that, at 10 m height above bottom, the frame was above the dynamic influence of all but the largest currents observed.

The sounds registered by the hydrophone are the primary focus of this thesis. However, due to the lack of prior measurements of, and theory for, the properties of the sound produced by turbidity currents, supporting, independent, measurements were needed. These independent measurements of the turbidity currents were needed to confirm the turbidity currents as sound producers, and to provide the turbidity current properties needed to predict theoretical sound pressure spectra for turbidity current noise. The two frame-mounted M3 multibeam sonars produced imagery (via changes in acoustic backscatter) that provided measurements of the turbidity current speed, thickness, and width. The *Heron* was also equipped with active sonars: two Knudsen single-beam sounders, and a Kongsberg EM710 multi-beam sonar. These ship-mounted instruments imaged the entire water column below the vessel, providing further measurements of the turbidity currents, and associated phenomena (e.g. bubble releases and SGN), at a range of acoustic frequencies (28 kHz, 70 - 100 kHz, and 200 kHz). Suspended 10 m above the bottom, on a single line, from the aft mooring float was a downward-looking, RDI Workhorse, acoustic Doppler current profiler (ADCP). This instrument was intended to measure a profile of the fluid velocities associated with the passage of the turbidity currents. Finally, a conductivity-temperature-depth sensor (CTD), mounted on a Moving Vessel Profiler

(MVP), was periodically lowered from the boat, and continuously profiled from the bottom to 10 m above, during the passage of turbidity currents.

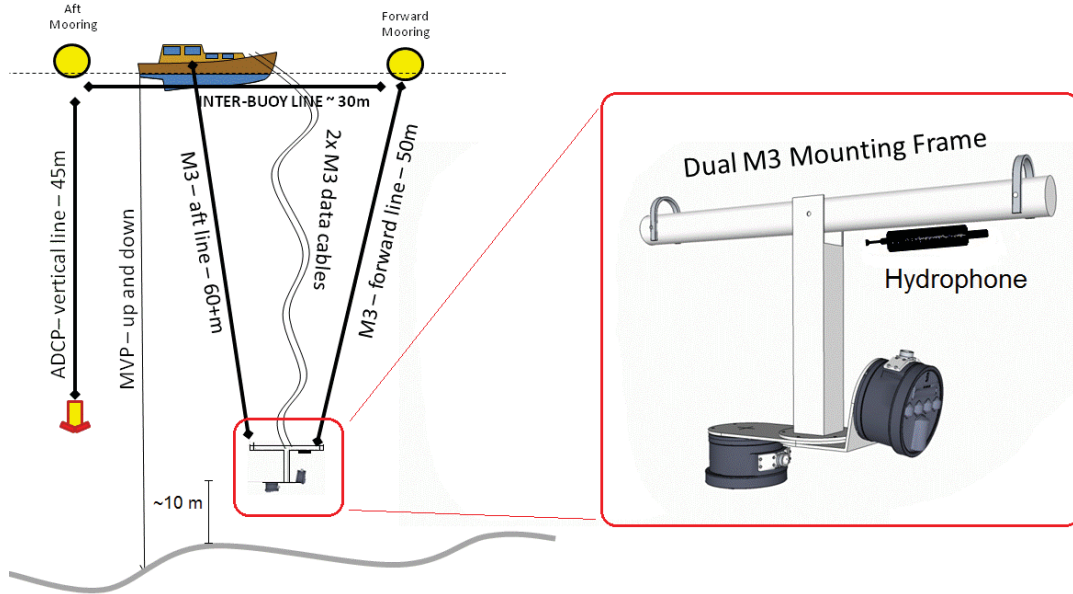


Figure 2.2: Vessel mooring and instrument frame diagram. (Courtesy of John Hughes Clarke).

## 2.2 Data Sources

In order to measure passive acoustic noise associated with turbidity currents, data from a single hydrophone was collected and analysed. However, as mentioned in the preceding section, many other types of data were recorded; the goal of which was to provide supporting information about turbidity current, and associated sediment (both suspended and bedload) properties. This section describes the instruments used, methods of data collection, and types of processing performed; for the passive acoustic, and all other supporting measurements.

### 2.2.1 Hydrophone

The icListen HF omni-directional hydrophone was configured to continuously record internally, at a sampling rate of 512 kHz (giving a theoretical maximum detectable frequency

of 256 kHz), for the duration of the frame deployment each day. The hydrophone data were Fourier transformed into the frequency domain with a frequency resolution of 1 kHz. Ensemble-averaged spectra were recorded at 0.0105 s intervals. By far the most dominant signals in the record were those of the active sonars aboard the *Heron* (Figure 2.3a). The relatively short transmit pulse duration of the active sonars allowed the identification, and removal, of spectra from the record which were highly contaminated with active sonar noise. The remaining spectra were averaged in 0.252 s intervals, resulting in unequal numbers of realizations averaged together. The percentage of spectra removed varied from about 10 – 40 % for two minute segments of data. An example of a record collected during the passage of a turbidity current demonstrates that this procedure largely removed active sonar noise from the spectrogram (Figure 2.3). All of the hydrophone data presented were processed in this way.

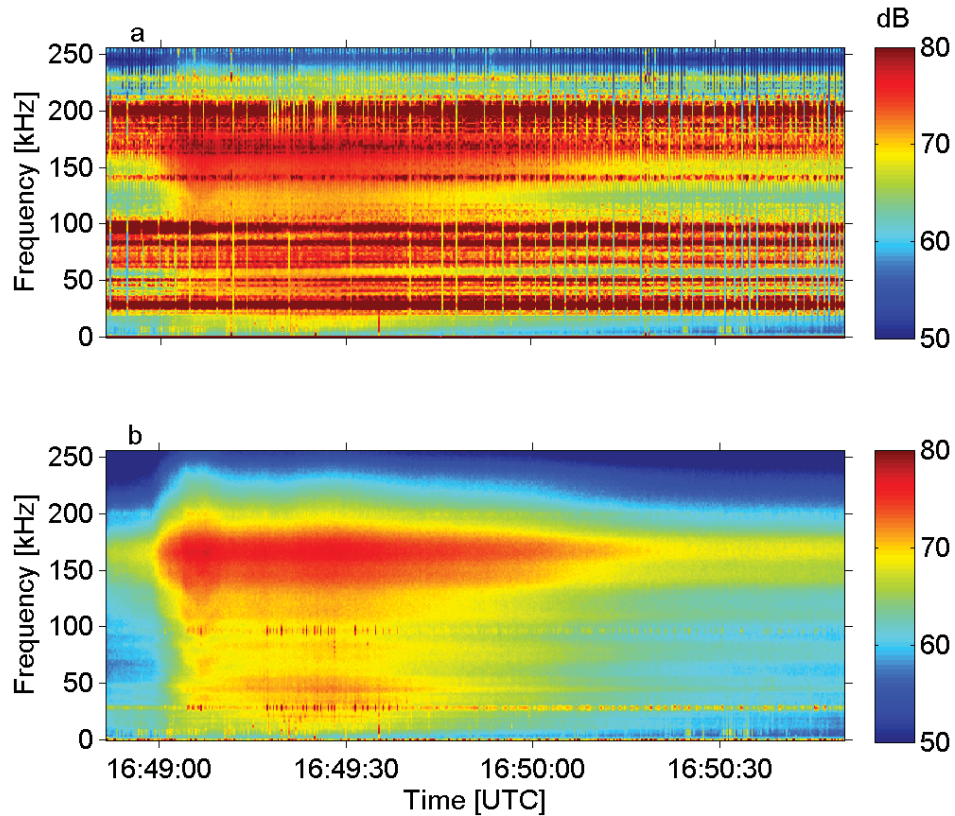


Figure 2.3: Hydrophone spectrograms from data collected in Howe Sound on 21 June, 2013 (not calibrated for instrument response). The colourscale represents dB (re  $1 \mu\text{Pa}/(\text{Hz})^{1/2}$ ): (a) before the active sonar noise removal procedure and (b) after. Both have a time resolution of 0.252 s. Event 172C.

### 2.2.2 M3 Multi-Beam Sonars

The two Kongsberg Mesotech M3 multibeam sonars, operating at 500 kHz, recorded backscatter amplitude as a function of range, covering a swath of 120 degrees, and sampled at a rate of 2 Hz (see Table 2.1 for resolution information). One instrument was aimed up-slope with the swath plane nearly horizontal, giving a view of currents approaching the frame. The second was aimed directly downward with the swath plane aligned up/down-slope, in order to provide a side view of the vertical and axial structure of the current as it passed beneath the frame. The pronounced increase in backscatter amplitude (which, as will be shown, is due to the high suspended sediment concentrations in the head and body) associated with the turbidity currents, made the upper and lateral boundary easily discernable in the sonar imagery. The horizontally-aimed sonar gave

time/distance estimates for the turbidity current fronts, which were used to estimate head speeds. The vertically-aimed sonar provided measurements of turbidity current head, and body, thicknesses.

### 2.2.3 Knudsen Single-Beam Sounders and Kongsberg EM710 Multi-beam Sonar

The two ship-mounted Knudsen single-beam echo-sounders—one operating at 28 kHz and the other at 200 kHz—recorded at variable profile sampling rates (see Table 2.1 for resolution information) and ran continuously while the *Heron* was 4-point moored. The ship-mounted EM710 multibeam sonar also continuously recorded during the time *Heron* spent at the mooring. It operated in the frequency range 70 – 100 kHz, with a sampling rate of 3.3 Hz and a range resolution of 5.4 cm. These instruments measured backscatter amplitude as a function of range, and provided information—through the full water column—about phenomena associated with the turbidity currents, e.g. suspended sediment, and the rising bubbles released from the bottom sediments by the passage of turbidity currents.

### 2.2.4 Acoustic Doppler Current Profiler

The *Heron's* stern line was connected to the two aft anchor rodes at a large float. A 1200 kHz RDI Workhorse acoustic Doppler current profiler (ADCP) was suspended from this float, at a height of about 10 m above the sea floor, and oriented so that the beams were directed downward. The ping rate was 2.5 Hz, and 10 pings were ensemble averaged to produce a profile, Table 2.1 gives the time and range resolution of the data. Velocity estimates were collected, pre-processed onboard the instrument in East, North, Up (ENU) coordinates, and recorded internally. A transformation was performed into down-channel and cross-channel coordinates, with positive  $U$  being in the down-channel (also down-slope) direction.

Instrument	Operating frequency [kHz]	Profile sampling rate [Hz]	Range resolution [cm]
M3 sonars	500	2	1.51
Knudsen sounders	28 and 200	$\simeq 1/4$ to 3	6.25
ADCP	1200	1/4	25

Table 2.1: Sonar and ADCP operating frequencies and resolutions.

## 2.2.5 Grab Sample and Sediment Grain Size

On the final day of the experiment two grab samples were taken at the mooring site. These samples were sieved to obtain the grain size distribution following the method outlined in *Ingram (1971)*. Figure 2.4 shows the grain size distribution and the settling velocities, as calculated by the method outlined in Appendix B, for the sediment samples taken from the field site.

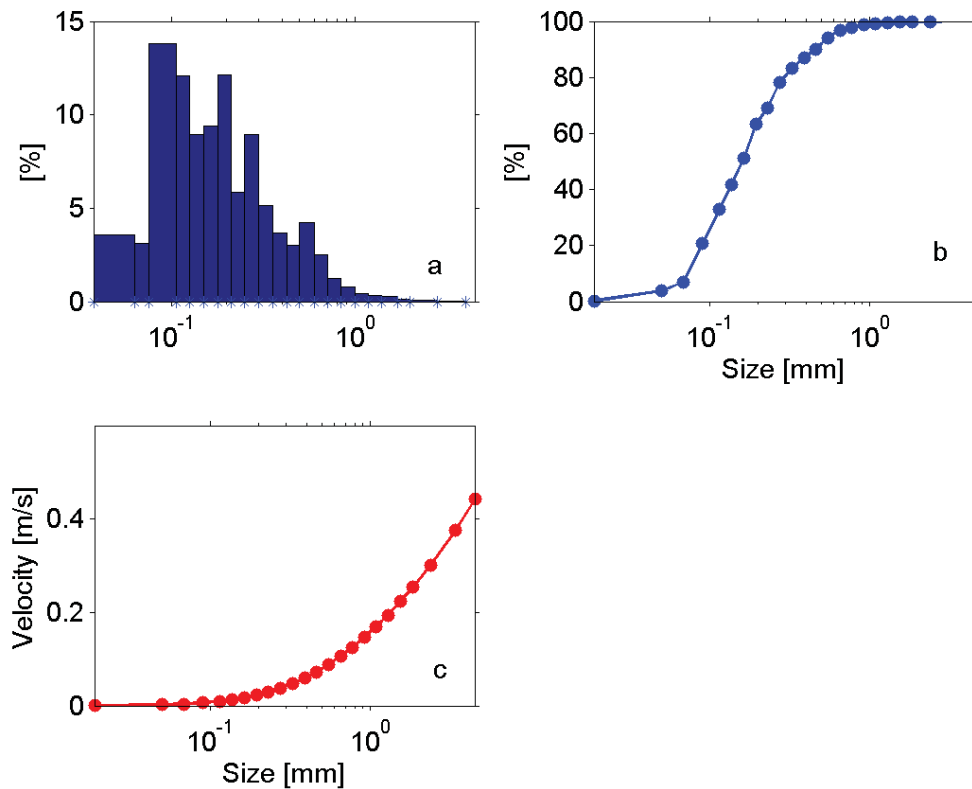


Figure 2.4: (a) Grain size distribution, (b) Grain size cumulative weight percent and (c) settling velocities for sediments in the grab samples taken at the instrument site.

The median equivalent spherical diameter ( $D_{50}$ ) for this distribution is  $162 \mu\text{m}$ , and the  $D_{90}$  (the size below which 90 % of the sample's mass is contained) is  $491 \mu\text{m}$ . The grain size distribution is uni-modal, containing sands predominantly in the medium to fine sand size classes.

### **2.2.6 Sound Speed Measurements**

Once during the 5 day field experiment an Applied Microsystems Limited (AML) sound velocity profiler was deployed in order to get a measurement of the sound speed profile. Additionally a Brooke Ocean Moving Vessel Profiler (MVP), to which was attached an AML underway Conductivity Temperature Depth (uCTD) sensor, was periodically profiled from the vessel, and CTD data were used to compute sound speed. These measurements of the sound speed profile were used in a ray-tracing model, investigating the propagation effects on a near-bottom sound source, on a sloping bottom. This relates to the question—presented in the introduction—of the cause of the measured temporal asymmetry in the turbidity current noise, detected by the hydrophone.

---

# CHAPTER 3

---

## THEORY

Multiple turbidity currents were detected during the field experiment, and hydrophone measurements confirmed that they generated sound. In order to determine whether the mechanism by which these currents produce sound is SGN, the theory describing how sound is generated by particle collisions is outlined in this chapter. To apply the theory for sound generation by particle collisions to turbidity current noise requires estimates of particle concentration, particle size, and particle collision velocity. These quantities are governed by the dynamic connections between flow speed and sediment concentration. The semi-empirical relationships among these turbidity current properties, and the associated theoretical background, are also presented. In addition, the theory for sound propagation through water with suspended sediment is presented, as it is used to account for sound attenuation along the path from the source region, within the turbidity current, to the hydrophone. Finally, the theory describing at what frequency bubbles freely oscillate, and hence generate sound, is also presented.

### 3.1 Turbidity Currents

Turbidity currents are a subset of gravity currents. In the case of turbidity currents, the gravitational force comes from a difference in density between the fluid within the current, and that surrounding it. This density difference is caused by suspended sediment within the current.

For the case of the body of a density current, with a constant source, moving through an unstratified ambient fluid, down a constant slope  $\Theta$ , the two-dimensional momentum equation is of the form (e.g. *Stacey and Bowen (1988)*),

$$\frac{\partial u}{\partial t} + \frac{\partial}{\partial x}(u^2) + \frac{\partial}{\partial z}(uw) = g \sin \Theta \frac{(\rho_t - \rho)}{\rho} + \frac{1}{\rho} \frac{\partial \tau}{\partial z} \quad (3.1)$$

where  $x$  and  $z$  are defined parallel and perpendicular to the slope,  $u$  and  $w$  are the corresponding velocities,  $\rho$  and  $\rho_t$  are the respective densities of the ambient fluid, and the fluid in the density current, and  $\tau$  is the local stress. The Boussinesq approximation has been applied to Equation 3.1, hence only density differences multiplied by  $g$  are included. Following many prior analyses (e.g. *Ellison and Turner (1959)*, *Plapp and Mitchell (1960)*, and *Johnson (1962)*), down-slope gradients in the pressure field are assumed small, as are all properties in the cross-current ( $y$ ) direction. Also, integrating vertically, taking the current to be in a steady state, ignoring advective terms, assuming the flow is longitudinally invariant and steady, ignoring entrainment and assuming bottom stress to dominate and be parameterized as  $\tau_b = \rho C_D U^2$ ; Equation 3.1 reduces to the Chezy equation

$$C_D U^2 = g' h \sin \Theta \quad (3.2)$$

with  $h$  being the thickness of the current body and  $g'$  the “reduced gravity”,

$$g' = \frac{\Delta \rho}{\rho} g \quad (3.3)$$

A more detailed treatment of the theory can be found in *Stacey and Bowen (1988)*. A graphical representation is shown in Figure 3.1.  $U_0$  is the frontal head speed,  $U$  is the speed of the body of the current,  $h$  is the thickness of the turbidity current body,  $h_0$  is the thickness of the head, and  $H$  is the water depth.

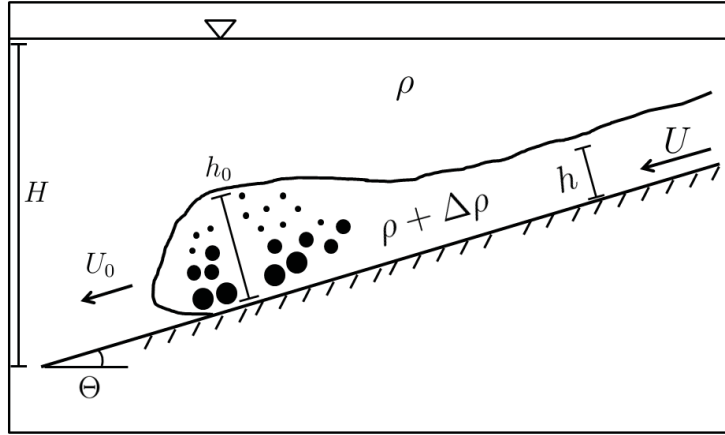


Figure 3.1: The anatomy of a turbidity current.

Empirical evidence has shown the head speed,  $U_0$ , of currents to be less than that of their body,  $U$ . The head speed of a gravity current fed by a constant source on a horizontal bed has been proposed by *Keulegan* (1957) to be

$$U_0 = A_{fr} \sqrt{g'h_0} \quad (3.4)$$

where  $A_{fr}$  is a non-dimensional number; *Keulegan* suggested a value of 0.75 for  $A_{fr}$  whereas *Simpson* (1997) has suggested 0.60.

### 3.1.1 Froude Number

More generally, and similar to  $A_{fr}$ , the Froude number is defined as the ratio of inertial force to gravitational force. For gravity currents on flat bottoms, this non-dimensional number takes the form:

$$Fr = \frac{U_0}{\sqrt{g'h}} \quad (3.5)$$

A relationship between this and the fraction of turbidity current thickness over water depth ( $h/H$ ), under various conditions of mixing and friction, is recognized (*Simpson* (1997)). Depending on the water depth, and the relative contributions of mixing and friction, the value for  $Fr$  has been empirically shown to be generally between 0.6 and 2 (*Simpson*

(1997)).  $Fr$  here is equivalent to  $A_{fr}$ , in Equation 3.4, except  $Fr$  here is for the body (thickness  $h$  as opposed to  $h_0$ ). Flows with  $Fr$  exceeding 1 are supercritical, and are in a regime where inertial forces dominate gravitational forces. The free interface no longer has the usually relatively strong gravitation force to stabilize it, and wave breaking and turbulence production at the interface—to dissipate energy—become common features. In this work the relationships, shown graphically by *Simpson* (1997), between  $Fr$  and the ratio of turbidity current thickness to water depth will be used to infer  $\Delta\rho$  and hence sediment volume concentration within the current.

Defining  $u_* = C_D U^2$ , and combining Equation 3.5 with Equation 3.2, an expression for the friction velocity  $u_*$ —for the body—is obtained.

$$u_*^2 = \left( \frac{U_0}{Fr} \right)^2 \sin \Theta \quad (3.6)$$

The flow speed,  $U_0$ , of the head is slower than that of the body,  $U$ , due to the need for ambient fluid to be displaced as the turbidity current front progresses. For gradual slopes  $< 5^\circ$  the head height,  $h_0$  is usually larger than the body thickness,  $h$ . As bottom slope ( $\Theta$ ) increases—to values between  $5^\circ$  and  $90^\circ$ —empirical evidence from lab experiments suggests that the head speed remains constant, for constant volume flux,  $Q$ , feeding the current (*Simpson* (1997)). Mixing in the body increases and body thickness,  $h$ , becomes larger, with larger slope.

$$\frac{U_0}{(g'Q)^{\frac{1}{3}}} = 1.5 \pm 0.2 \quad (3.7)$$

$Q$  is taken as the integral of  $U$  in the body, from the bottom to the top boundary of the current. This result implies the existence of a self-regulating mechanism, whereby mixing in the body increases with bottom slope.

These non-dimensional relationships, along with measurements, are used to infer characteristic flow speeds (e.g.  $u_*$ ), and sediment concentrations ( $g'$ ) associated with detected turbidity currents.

### 3.1.2 Sediment Size Distribution within Turbidity Currents

In steady channel flow the Vanoni distribution describes the vertical profile of sediment concentration, as a function of particle settling velocity (*Fredsoe et al.* (1995)). This distribution is characterized by more larger particles nearer to the bottom. This is of some

relevance to the vertical structure of sediment concentration within a turbidity current. The Vanoni distribution gives concentration  $C_v$  as a function of  $z$  (depth)

$$C_v = C_{vb} \left( \frac{H - z}{z} \frac{b}{H - b} \right)^{w_s / (\kappa u_*^2)} \quad (3.8)$$

where  $w_s / (\kappa u_*^2)$  is the Rouse parameter,  $w_s$  the particle settling velocity,  $\kappa$  von Kármán's constant, and  $C_{vb}$  is the reference concentration, given at a height  $b$  above the bed. In steady channel flow  $H$  is the water depth, but in the case of turbidity currents would be taken as the thickness of the current body.

### 3.1.3 Bedload

High velocity flows have the ability to mobilize large quantities of mobile material. Under these conditions of high sediment concentration, a concentrated bedload layer is expected (*Nielsen (1992)*). Particle collisions associated with turbidity currents are more likely to occur in this concentrated near-bed layer, as opposed to the lower concentrations in the interior of the turbidity current.

The Shields parameter ( $\theta_s$ ), and critical Shields parameter ( $\theta_{sc}$ ) are defined as

$$\theta_s = \frac{u_*^2}{(\sigma - 1)gd} \quad (3.9)$$

where  $d$  is the particle diameter,  $\sigma = \rho_s / \rho$  is the specific gravity of the particle material, with  $\rho$  being the density of the ambient fluid. The Shields parameter represents a measure of shear stress over gravitational force.  $\theta_{sc}$  represents a critical value for the Shields parameter, for which grains are able to be mobilised by the shear stress associated with the flow. Studies have empirically shown that  $\theta_{sc}$  is relatively constant for nearly spherical grains, and can be chosen to be  $\theta_{sc} = 0.05$  (*Nielsen (1992)*). In the Results, the value of the Shields parameter is estimated to be much greater than  $\theta_{sc}$ , and also much greater than unity. It can therefore be assumed that the bedload transport is in the sheet flow regime, which has implications for the model of sound generation by particle collisions.

Bedload layer thickness is estimated by *Nielsen (1992)*, assuming steady flow, as

$$L_B = 2.5(\theta_s - \theta_{sc})d \quad (3.10)$$

$L_B$  represents the thickness the bedload layer would be at rest (i.e. with a concentration  $C_{vmax}$ ). A reasonable estimate, used here, for  $C_{vmax}$  for near spherical grains is 0.65

(Nielsen (1992)). Choice of a concentration in the mobile bedload layer,  $C_{vbl}$ , allows a mobile bedload layer thickness ( $z_{bl}$ ) to be calculated.

$$z_{bl} = \frac{C_{vmax}}{C_{vbl}} L_B \quad (3.11)$$

## 3.2 Sediment Generated Noise (SGN)

A primary goal of this thesis is to determine whether sound from particle collisions (SGN), associated with the turbidity currents, is responsible for the measured passive acoustic signal. *Thorne* (1985,1986) showed that, in an aqueous environment, the sound produced by colliding bodies is mainly rigid-body radiation. The acoustic pressure wave generated by a collision was not a result of resonant elastic vibrations within the body, but rather due to the compression and rarefaction of the surrounding fluid, caused by the acceleration of the body as a whole. The radiated acoustic pressure as a function of time is described fully by:

$$p(t, r, \theta) = \int_0^\zeta P_i(\xi, r, \theta) A(t - \xi) d\xi \quad (3.12)$$

where  $A$  is the acceleration time history of the rigid body. The integral is evaluated for time 0 to  $\zeta$  via the integration variable  $\xi$ , and  $P_i$  is the analytic solution for the impulse response pressure (*Akay and Hodgson* (1978a)). Equation 3.12 represents a convolution between the impulse response, and the acceleration time history of a sphere in fluid. Thus, if the acceleration time history of a sphere is known, then the resulting pressure field it creates can be obtained. In particular, if the collision is assumed to be Hertzian (*Akay and Hodgson* (1978a)), then the acceleration time history can be represented mathematically, yielding analytic solutions for the pressure field (*Thorne and Foden* (1988)). Using the convolution theorem, the spectrum of the pressure field can be written

$$F[p(t, r, \theta)] = P(f, r, \theta) = F[P_i]F[A] \quad (3.13)$$

where  $F$  is the Fourier transform operator.

Laboratory measurements (*Thorne* (1985)) have shown good agreement between rigid body radiation theory and the sound-field created by many collisions of glass spheres,

caused by them falling over one another in a rotating drum. Important results are that the peak frequency of sound is inversely proportional to the sphere diameter, and the total sound pressure level is predominately a function of the number of collisions occurring. Collision velocity mainly affects sound pressure level, it also affects the frequency of the radiated sound, but to a lesser degree.

In a later study, *Thorne* (1986) used the same laboratory set-up with natural sand of various sieved sizes, and obtained results similar to the glass sphere experiment, by using the spherical equivalent diameter of the natural grains. This indicates that the sound produced in this rigid body collision framework is relatively insensitive to particle shape.

*Thorne* (1986) predominantly focused on particles of just one size. Using the theory outlined in Appendix A an expression for a frequency ( $f_t = 1/2t_0$ ), representative of a peak frequency, can be obtained;  $t_0$  (Equation A.3) is the contact time for a collision. For two identical spheres this is

$$f_t = 0.0855[E/\rho_s(1 - \nu^2)]^{0.4}(U_c^{0.2}/a) \quad (3.14)$$

where  $\rho_s$  is the density of the particle material,  $E$  is Young's modulus,  $\nu$  is Poisson's ratio,  $U_c$  is the impact velocity and  $a$  is the particle radius. Further, peak pressure generated by an impact was empirically estimated by *Akay and Hodgson* (1978a) as

$$P_{PK} \approx 1.29 \times 10^{-6} E(a/r_p)^{1.07} (U_c/c_a)^{1.25} \sqrt{Z_w/Z_a} \quad (3.15)$$

where  $r_p$  is the distance from the collision,  $c_a$  is the sound speed in air,  $Z_w$  and  $Z_a$  are the acoustic impedances of water and air respectively.

To determine total pressure levels ( $P_T$ ), an estimate of the number of collisions occurring is necessary. Assuming that the source pressures from different collisions are uncorrelated, for  $m$  independent sources:

$$P_T^2 = \sum_{i=1}^m P_i^2 \simeq M P_i^2 \quad (3.16)$$

where  $M$  is the total number of collisions.

### 3.2.1 Predicted Spectrum for Idealized Two-Particle Collisions

The previous analysis considered only collisions between particles of the same size, and focussed on a characteristic peak frequency. Passive acoustic measurements collected in

the field experiment were presumably from collisions between particles of many different sizes, as such, information on spectral shape is of value in this case. Figure 3.2 illustrates a set-up for which the rigid body radiation sound pressure field has an analytical solution, as outlined in Appendix A. In two dimensions the field point coordinate is  $(r, \theta)$ . The impactee is assumed to be initially stationary, and the impactor makes a direct collision travelling at speed  $U_c$ , where  $a_i$  and  $a_j$  represent the sphere radii.

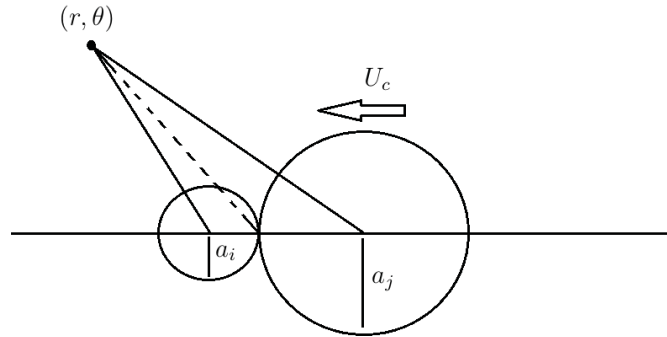


Figure 3.2: Diagram of a collision for which the SGN is analytically solvable.

Example of spectra from the analytical solution, at  $r = 1$  m, are shown in Figure 3.3 for different values of particle radius  $a$ , and collision speed  $U_c$ . The angular dependence of total spectral sound pressure level is also plotted in Figure 3.3b. Sound from collisions of this type is strongly forward-directed. Frequency is predominantly dependent on particle size, while sound pressure level depends mainly on impact velocity.

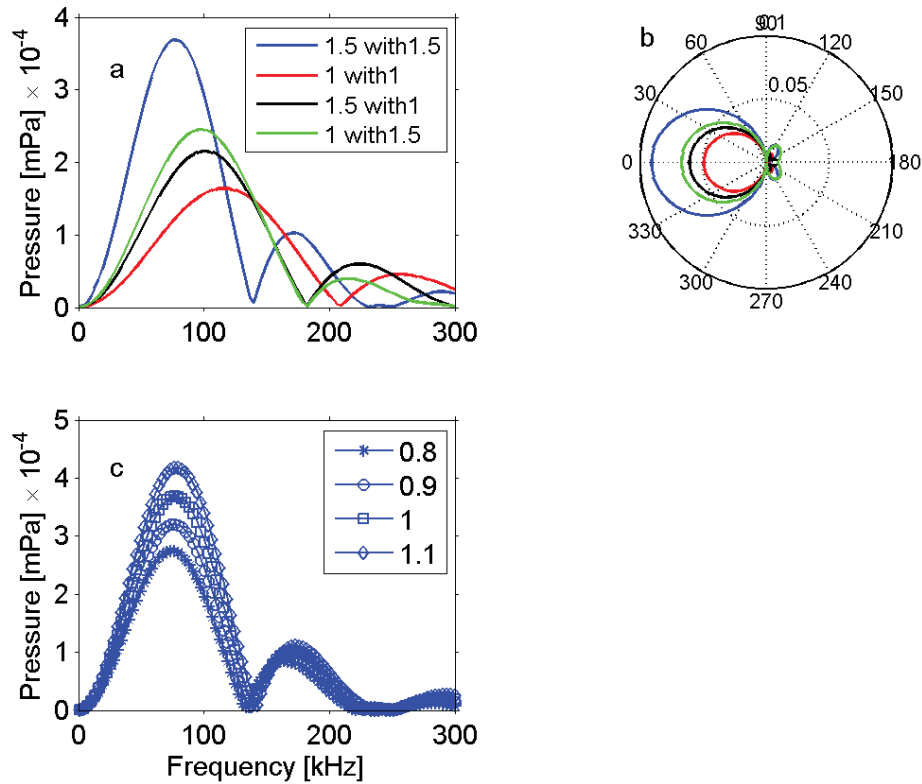


Figure 3.3: Analytical solutions of spectra from some simple collisions. (a) Spectra when different size spheres are collided at the same speed, the legend indicates particle size  $a_j$  colliding with  $a_i$ , in mm. (b) Total spectral pressure levels for the collisions in (a) versus  $\theta$ . (c) Spectra from collisions between equal sized particles (1.5 mm) versus collision speed. Collision speeds are shown in the legend in m/s.

### 3.2.2 Particle Collision Frequency

If the sound measured at the receiver—originating from turbidity currents—is assumed to be a sum of contributions of sound from individual collisions, then the size of particles colliding, and the frequency at which they collide are important. Because bedload transport is in the sheet flow regime, the particle tumbling scenario in the rotating drum experiments, carried out by *Thorne* (1985), is not appropriate here. Instead, the particles are assumed to be colliding within a thick sheet flow layer, in which the particle volume concentrations are of order 10%. For these conditions, the particle collision frequency is estimated based on the theory of random collisions in an ideal gas. The grainsize distribution is divided into  $n_s$  size classes. For collisions between particles in size class  $j$ , assumed to be travelling

with speed  $U_c = 2u_*$ , and particles in size class  $i$ , assumed to be stationary, the effective weighting for sound produced from collisions is made up of two parts: i) The likelihood of collision based on the size of each particle and the impact velocity, and ii) the number density of each of the two size classes of particles involved in the collision. This follows from the ideas of mean free path and collision frequency, outlined in the kinetic theory of gases (*Serway (1990), 577-578*). A spherical particle, of radius  $a_j$ , moving at speed  $U_c$  through space occupied by stationary spherical particles, of radius  $a_i$  (black circles in Figure 3.4), results in a volume per unit time where collisions may occur of  $U_c\pi(a_i + a_j)^2$ . This is illustrated in Figure 3.4 by the grey shading.

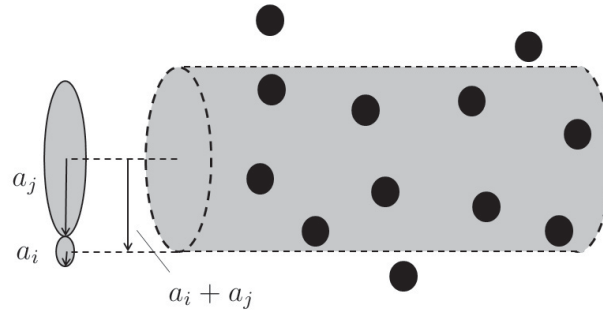


Figure 3.4: Diagram of the collision volume for a moving particle.

Multiplication of this volume by the number density,  $n_i$ , of particles in size class  $i$  gives the number of collisions occurring per unit time, on average, between one particle in size class  $j$ , and the particles in size class  $i$ . This is defined as the collision frequency of a single particle in size class  $j$ . Multiplication by the number density,  $n_j$ , of particles in size class  $j$  gives:

$$W_{ij} = U_c\pi(a_i + a_j)^2n_in_j \quad (3.17)$$

where  $W_{ij}$  represents the number of collisions per unit volume, per unit time, for all particles in size class  $j$ , colliding with all particles in size class  $i$ ;  $a$  and  $n$  are the particle

radius and number density respectively. In equation 3.17, a factor of  $1/\sqrt{2}$  is omitted (due to its insignificance relative to the concentrations of particles,  $n$ ) from the classical collision theory as outlined in *McNaught and Wilkinson (1997)*. Importantly, as results will show, collision frequency is proportional to the square of particle concentration.

The majority of particles in the sheet flow layer will be large enough to fall out of suspension, and spend most of their time at, or near, the bottom of the current, where particle concentrations are highest. The Vanoni distribution (see Section 3.1.2), with increasingly more larger sized particles nearer the bottom of the current, supports this argument. The work presented here does not use the Vanoni distribution directly; instead, a simplified approach is used which reduces the set of particles involved in noise creating collisions to those that have a settling velocity greater than a chosen cut-off. The assumption then is that all particles with settling velocities less than this cut-off (smaller particles) remain in suspension in the turbulent interior of the current, and undergo no sound producing collisions, while those with settling velocities larger (larger particles) remain confined to a bedload layer and undergo collisions.

Collisions are assumed to occur throughout the bedload layer. The field point distance ( $r_0$ ) for the sound from individual collisions is taken to be equal to the bedload layer thickness  $z_{bl}$ , and the sound intensity is averaged over all field point angles  $\theta$ . The sound produced by the bedload layer is then given by

$$P_0^2 = \sum_{i,j=1}^{n_s} W_{ij} P_{ij}^2 \quad (3.18)$$

where  $P_0^2$  is assumed to be emitted per unit area, per unit time, at a reference height  $z_0 = r_0/2$  above the top of the bedload layer.

### 3.3 Bubble Noise

The ship-mounted acoustic instruments detected bubbles associated with the passage of turbidity currents. These bubbles were observed to be released from the sea-floor sediments coinciding with the passage of a turbidity current head, and remained in the water column for O(10) min; they therefore require consideration in this context. Bubbles are known to be important in the marine acoustic environment, both as sources and scatterers of sound. This work takes bubbles into account as sound sources.

As a first approximation bubbles can be treated as simple harmonic oscillators (*Leighton* (2012)). In the ocean environment there are a multitude of pressure waves present that can act as impulse forcing to start, and maintain, the bubble oscillating. This thesis assumes that bubbles in the water column are continually radiating sound at their resonant frequency. This frequency, known as the Minnaert frequency, is

$$f_b = \frac{1}{2\pi a_b} \sqrt{\frac{3\gamma p_h}{\rho}} \quad (3.19)$$

where  $\gamma$  is the specific heat ratio  $c_p/c_v$ ,  $p_h$  is the hydrostatic pressure,  $a_b$  is the equilibrium bubble radius, and  $\rho$  is the density of the surrounding water.

### 3.4 Sound Propagation Effects

Field measurements of noise generated by turbidity currents—occurring over a large area, and with varied environmental conditions—was obtained solely from one omnidirectional hydrophone. Knowledge of how the sound is affected as it travels from source to receiver—through the medium—is required, specifically as it travels through water containing suspended sediment.

The frequency dependent losses as sound passes through a three dimensional medium constitutes a complex problem. Many factors contribute to the sound field observed at a point: attenuation due to the medium, scattering/absorption by particles in suspension, reflection and refraction within the medium and at boundaries, and the number and properties of sources, etc. Due to the relatively high frequencies dealt with in this work (i.e.  $> 20$  kHz) sound propagation from source to receiver can be treated using ray theory.

#### 3.4.1 Ray Tracing Model

In order to estimate the potential effects on the turbidity current sound signal, as it travels to the receiver from distant ( $> 50$  m) sources; this thesis makes use of the already existing ray tracing model: BELLHOP (*Porter and Liu* (1994)). Ray-like beams are traced from the source using the ray equations

$$\frac{dr}{ds} = c\hat{\xi}(s), \quad \frac{d\hat{\xi}}{ds} = -\frac{1}{c^2} \frac{dc}{dr} \quad (3.20)$$

$$\frac{dz}{ds} = c\hat{\zeta}(s), \quad \frac{d\hat{\zeta}}{ds} = -\frac{1}{c^2} \frac{dc}{dz} \quad (3.21)$$

where  $c$  is the sound speed,  $r(s)$ ,  $z(s)$  is the trajectory in cylindrical coordinates,  $(\hat{\xi}(s), \hat{\zeta}(s))$  is a tangent to the beam, and  $s$  is the along-beam coordinate. The initial conditions define the source location, and launch angle of the emitted beam:

$$r(0) = r_s, \quad \hat{\xi}(0) = \frac{\cos \Phi}{c(0)} \quad (3.22)$$

$$z(0) = z_s, \quad \hat{\zeta}(0) = \frac{\sin \Phi}{c(0)} \quad (3.23)$$

where  $(r_s, z_s)$  is the source location, and  $\Phi$  is the ray take off angle.

Numerical solutions for each beam, and addition of squared pressure's from multiple beams from a source, can be used to estimate transmission loss at far field receiver points. For more detail see (*Porter (2011)*).

### 3.4.2 Attenuation

The intensity of plane waves propagating along a straight line path in a homogeneous medium is given by

$$I = I_0 e^{-2\alpha x} \quad (3.24)$$

with the sound intensity being defined by

$$I = \frac{P^2}{\rho c} \quad (3.25)$$

where  $\alpha$  is the absorption coefficient,  $I_0$  is the source level acoustic intensity, and  $x$  is the distance travelled through the medium. For seawater, the absorption coefficient,  $\alpha_w$ , is calculated using the empirical relationship given by *Fisher and Simmons (1977)*. For transmission of sound through turbid water, the additional attenuation due to the suspended sediment,  $\alpha_s$ , has contributions from viscous absorption and scattering. The relative importance of either factor is dependent on the value of  $ka$ , with  $a$  being the suspended particle radius,  $k = 2\pi/\lambda$  being the wavenumber, and  $\lambda$  the wavelength of the sound wave. For  $ka \ll 1$  *Urlick (1948)* has shown this coefficient to be

$$2\alpha_s = n\Sigma_T \quad (3.26)$$

where  $\Sigma_T$  is the total cross-section, and is defined as

$$\Sigma_T = \frac{4}{9}\pi k^4 a^6 + \frac{4}{3}\pi a^3 k(\sigma - 1)^2 \frac{S}{S^2 + (\sigma^2 + T)^2} \quad (3.27)$$

$$S \equiv \frac{9}{4\beta a} \left(1 + \frac{1}{\beta a}\right) \quad (3.28)$$

$$T \equiv \frac{1}{2} + \frac{9}{4\beta a} \quad (3.29)$$

where  $\beta = (\omega/2\eta)^{\frac{1}{2}}$ ,  $\omega = 2\pi f$ ,  $f$  is the acoustic frequency, and  $\eta$  is the kinematic viscosity.  $C_v$  is the fractional volume concentration of the suspended particles in the water, and is defined as:

$$C_v = \frac{4}{3}\pi a^3 n \equiv \frac{\Delta\rho/\rho}{\sigma - 1} \quad (3.30)$$

where  $n$  is again the number density of particles in suspension. In Equation 3.27 the first term represents losses due to scattering from the particles in suspension; the second term accounts for the loss due to friction arising from the relative motion of the fluid, and particles, under the forcing of the sound wave.

### 3.4.3 Hydrophone Listening Radius

The maximum radial distance at which sounds produced on the sea-floor can be detected by a hydrophone, suspended some distance above the sea-floor, is of importance to this work. In this context it has application to how far up-channel a turbidity current is likely to be heard, assuming a constant suspended sediment layer, as well as the sensitivity of the hydrophone to sound produced at the sea-floor as a function of slant angle, and distance. As a first approximation, assume a sea-floor emitting a given sound intensity, per unit area, at a reference height  $z_0$  above the top of the bedload layer,  $z_{bl}$ . Further, assume particles in suspension, with a volume concentration  $C_v$ , in a layer of thickness  $z_s$  above the sea-floor. This scenario is illustrated in Figure 3.5, where  $r, \theta$  are the spatial coordinates,  $z_h$  is the height of the receiver above the bed,  $R$  and  $\phi$  are the slant distance and angle from the area element  $dA$  to the receiver.

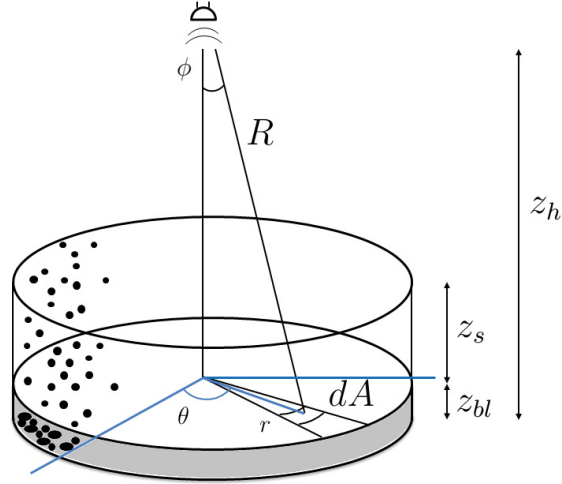


Figure 3.5: Diagram of the hydrophone listening radius.

Assuming only straight line paths from source to receiver, and that the only transmission losses are due to absorption by seawater, and scattering and absorption by the particles in suspension, the mean square sound pressure level at the receiver is given by

$$P^2 = P_0^2 \int \frac{e^{-(\Gamma/\cos\phi)}}{R} dA \quad (3.31)$$

where  $P_0$  is the pressure at a reference height  $z_0$  close to the bed and

$$\Gamma = 2(\alpha_w z_h + \alpha_s z_s) \quad (3.32)$$

The integral in Equation 3.31 can be solved analytically giving

$$P^2 = P_0^2 (\theta_2 - \theta_1) z_o^2 \left[ \ln \left( \frac{|\hat{y}_2|}{|\hat{y}_1|} \right) \sum_{j=1}^{\infty} \frac{(-\Gamma)^j (\hat{y}_2^j - \hat{y}_1^j)}{j \cdot j!} \right] \quad (3.33)$$

where  $\hat{y} = 1/\cos\phi$ , and the subscripts 1 and 2 represent the integration limits.

### 3.4.4 Inferring Sediment Concentration from Backscatter Intensity at Multiple Frequencies

For the purpose of comparison, an independent method of estimating suspended sediment concentration within the turbidity current was sought. This method was based on the differential attenuation of sound at two frequencies, as it propagates through water containing

suspended particles. If a sonar emits sound at a given frequency and receives it back at the same transducer; that sound is by definition backscattered. The intensity of backscattered sound, at frequency  $f$ , and range  $z$  is defined as

$$I_b = n(z) \frac{\sigma_b}{z^2} K_{TR} \exp \left( -4\alpha_w z - 2 \int_0^z n(z) \Sigma_T dz \right) \quad (3.34)$$

where  $n(z)$  is the number density of particles, as a function of range,  $\sigma_b$  is the backscattering cross-section,  $K_{TR}$  is the effective transceiver sensitivity; and it includes the transmit power and the integral over the transducer directivity.  $\Sigma_T$  is the total acoustic cross-section (scattering and viscous absorption). In highly turbid environments, particle scattering will likely be the dominant mechanism of backscatter. If the ratio of backscatter intensity, at frequency  $f_2$  to  $f_1$ , at range  $z_A$ , is subtracted from that at  $z_B$ , the following is obtained

$$\int_{z_A}^{z_B} n(\Sigma_{T_1} - \Sigma_{T_2}) dr = \chi \quad (3.35)$$

where

$$\chi = \frac{1}{2} \ln \left[ \frac{I_b(f_2, z_B) I_b(f_1, z_A)}{I_b(f_1, z_B) I_b(f_2, z_A)} \right] \quad (3.36)$$

Making the assumption that  $n$  is independent of  $z$ , the integral on the left hand side of Equation 3.35 can be evaluated, giving

$$n(\Sigma_{T_1} - \Sigma_{T_2})(z_B - z_A) = \chi \quad (3.37)$$

If  $\chi$  is plotted against  $(z_B - z_A)$ , then  $n(\Sigma_{T_1} - \Sigma_{T_2})$  represents the slope. If appropriate values for  $\Sigma_{T_1}$  and  $\Sigma_{T_2}$  are inferred—based on particle properties—then  $n$ , and hence  $C_v$ , can be estimated. Implicit in the use of backscatter intensity is the assumption that scattering from suspended particles dominates viscous absorption. This implies particles are of larger size classes, i.e. sands. A similar approach was pursued first by *Topping et al.* (2007) for larger size classes (sands). They also used attenuation to estimate concentration of the smaller size classes (silts and clay).

---

## CHAPTER 4

---

# TURBIDITY CURRENT PROPERTIES

This thesis is primarily concerned with noise produced by turbidity currents. However, of great importance to the creation of this noise are the dynamical properties of turbidity currents, including the associated sediment transport. This chapter presents these properties—both observed and inferred—with a focus on the properties that predominately influence particle collisions: that is, characteristic flow speeds, and sediment concentrations.

### 4.1 Overview

During the field experiment, 14 discrete turbidity currents passing beneath the instrument frame were identified. These events are designated by the Yearday on which they occurred, and a letter indicating the position in the sequence of events on the same day, i.e. the third observed event occurring on June 21 (Yearday 172) is labelled 172C. In this thesis event 172C is often focussed on as representative of the more intense events observed.

Figure 4.1 presents the time history of acoustic backscatter from the 200 kHz and 28 kHz single-beam sounders for event 172C. The horizontal axis indicates time, with 0 s designating the arrival of the turbidity current front directly below the instrument frame. The vertical axis is water depth. The greyscale indicates the intensity of backscattered sound in dB (arbitrary reference); lighter shades indicating higher amplitude received signal. The high amplitude return at 60 m depth—persisting for the entire record—is the reflection from the bottom, and that at roughly 50 m depth is the return from the instrument frame.

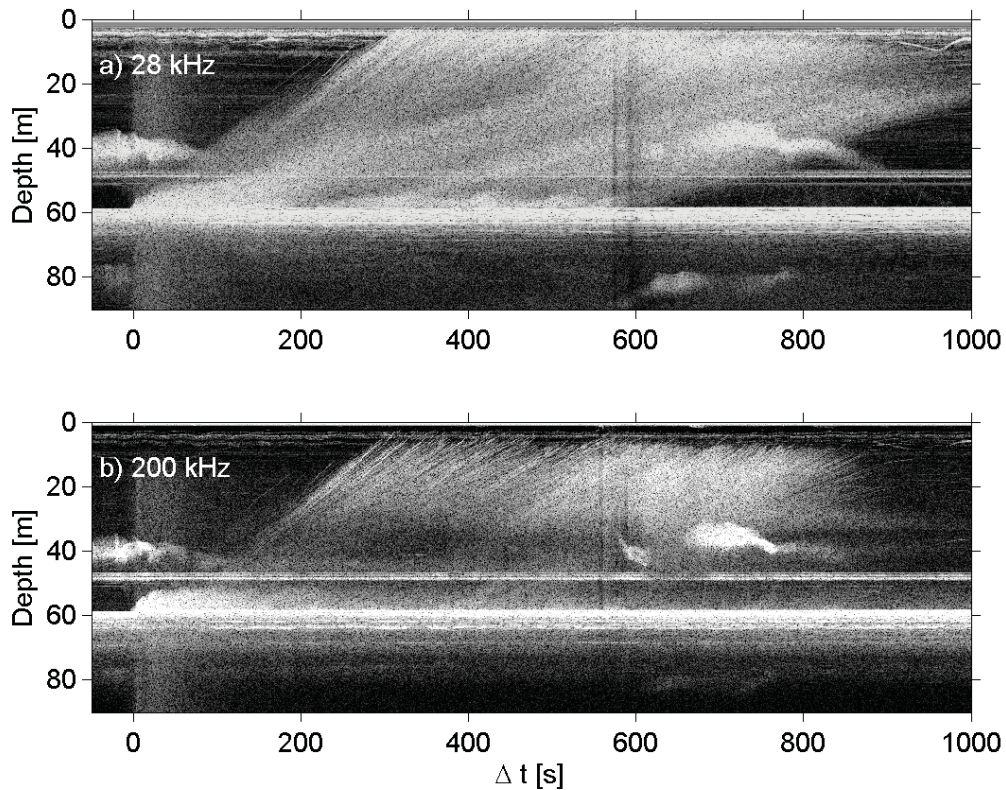


Figure 4.1: Knudsen single-beam sonder backscatter data in dB (arbitrary reference): (a) 28 kHz, and (b) 200 kHz. Event 172C.

The arrival of turbidity current 172C is evident as an abrupt increase in backscatter – at 200 kHz especially – in the region from the bottom to roughly 5 m height above the bottom. After the head and body have passed, i.e. after the first 50 s of the event, the backscatter in this depth interval steadily decreases as time progresses. The passage of the turbidity current also releases gas bubbles from the bottom, indicated by the relatively strong backscatter in diagonal streaks through the water column, which are more pronounced in the 28 kHz record. The strong near-bottom signal, associated with suspended sediment within the turbidity current, persists for roughly 200 s, and that associated with bubbles in the water column persists for about 900 s. During the first 50 to 60 s of the event there is also a lower intensity signal, in both the 28 kHz and 200 kHz records, which extends both above and below the bottom, and is relatively independent of range. This signal is turbidity current generated noise.

## 4.2 Bubble Sizes

Figure 4.2 shows a time series of the backscatter from the downward-looking beam of the ship-mounted EM710 multi-beam sounder, during the passage of turbidity current 172C. (The turbidity current generated noise is also evident in this frequency range, 70 - 100 kHz, in the time interval from  $\Delta t \simeq 0 - 80$  s).

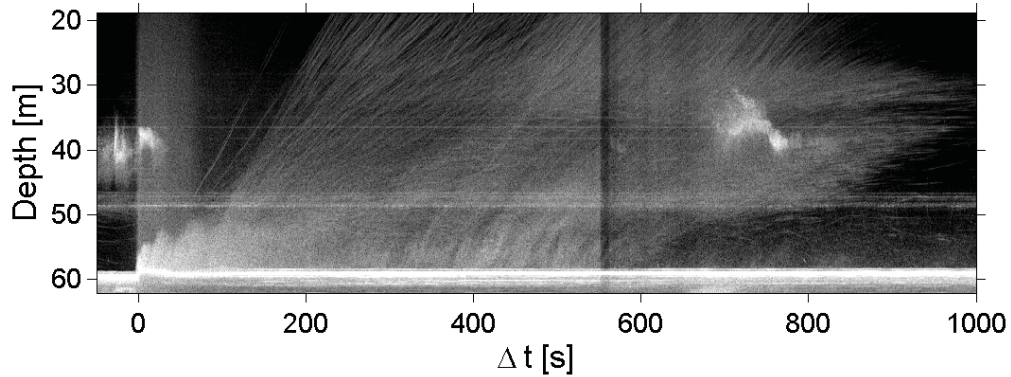


Figure 4.2: Acoustic backscatter time series from the vertical beam of the 70 - 100 kHz EM710 vessel-bottom mounted multibeam. The grayscale indicates dB (arbitrary reference). Event 172C.

Isolated bubble tracks are evident in the backscatter—particularly in the time interval  $\Delta t = 100$  to 400 s, and the depth range 20 to 40 m—as individual diagonal lines. These bubble tracks were approximated as straight lines, for which vertical displacement versus time measurements on 300 individual examples were used to determine constant bubble rise rates. These rise rates (Figure 4.3a) were then related to (spherical) bubble size, as outlined in Appendix B. Figure 4.3b shows the distribution of bubble sizes calculated in this manner, for event 172C. The small ( $< 2$  mm) sizes indicate that the spherical shape assumption is likely valid.

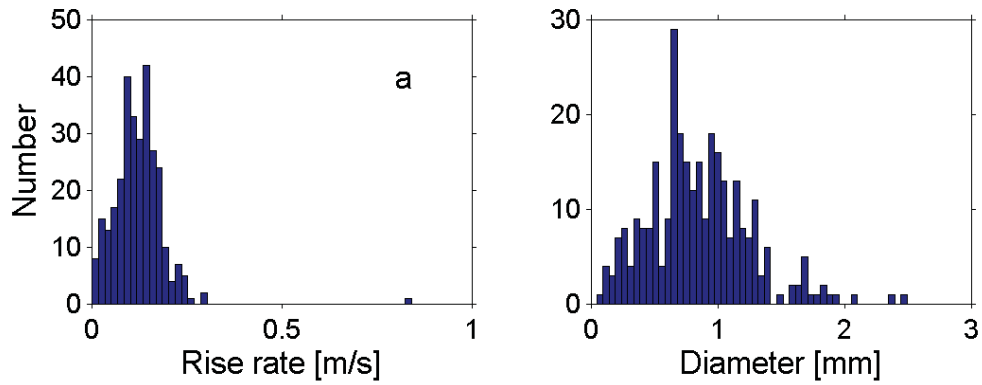


Figure 4.3: (a) Bubble rise rate, and (b) bubble diameter histograms for event 172C.

### 4.3 Head Properties

The backscatter imagery from the forward-looking M3 sonar was used to estimate turbidity current head speed and width. Figure 4.4 is typical of data from the forward-looking M3 during a turbidity current event. Cyclic steps with about 30 m wavelength are clearly visible on the channel floor. The turbidity current front, indicated by the arrow, can be seen approaching from about 1-o'clock, and at progressively closer distances in each image.

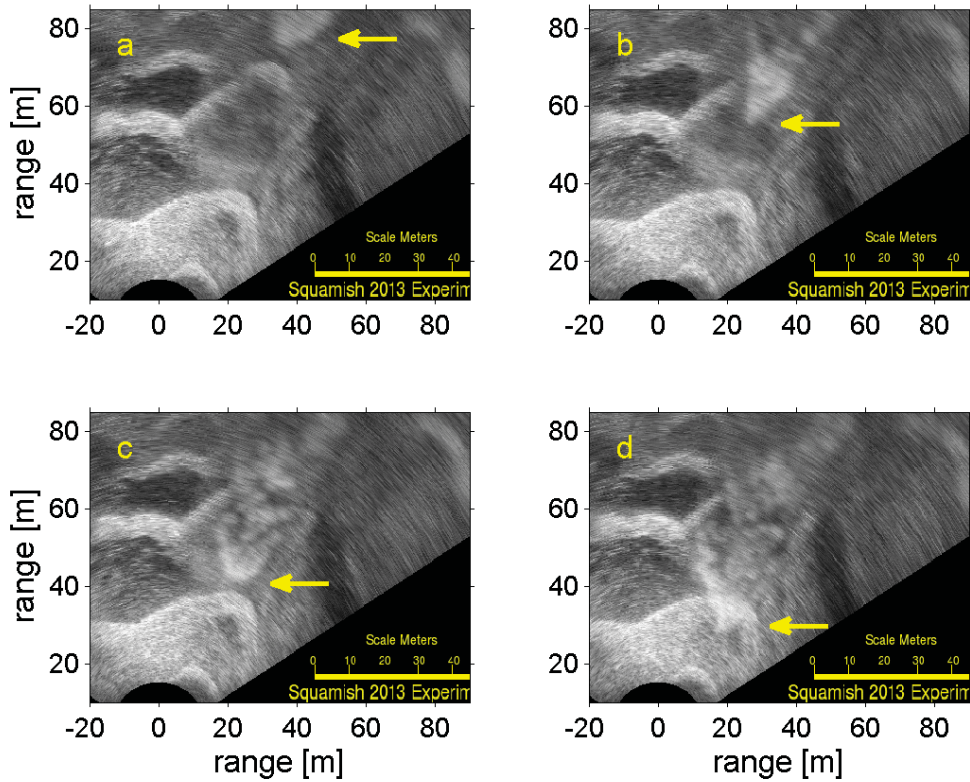


Figure 4.4: Backscatter at successive times (sequentially from (a) to (d), with the time between images  $\Delta t = 10$  s) from the forward-looking M3 sonar. The grayscale indicates dB (arbitrary reference). The turbidity current front is indicated by yellow arrows. Event 172A.

The slant range to the turbidity current front was converted to bed-parallel distance using a bottom slope of  $4.7^\circ$ , and the resulting distances at successive time intervals used to compute the turbidity current frontal velocities. The values for event 172C are plotted in Figure 4.5a, together with the best fit straight line, which indicates a linear decrease in head speed with time (and thus distance) from the instrument location.

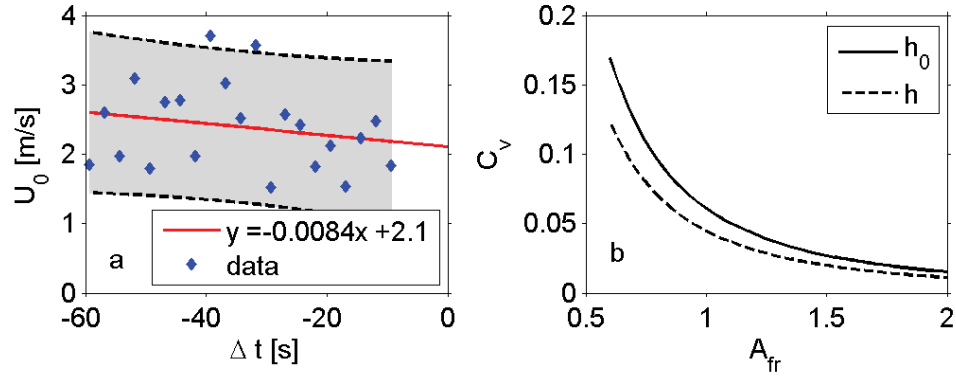


Figure 4.5: (a) Head speed as estimated from the M3 sonder, with a linear leastsquares best fit (red line, the grey shading indicates the 90% confidence interval) and, (b) suspended sediment concentration as a function of  $A_{fr}$  (or Fr) for  $U_0 = 2.1$  m/s at  $\Delta t = 0$  s calculated from Equation 3.4 with  $h_0 = 4.68$  m (solid line), and Equation 3.5 with  $h = 6.39$  m (dashed line). Event 172C.

Extrapolating the fit to  $\Delta t = 0$  s yields  $U_0 = 2.1$  m/s. The density difference,  $\Delta\rho$ , in the head was estimated using Equations 3.4 and 3.5, with head height ( $h_0$ ) and body thickness ( $h$ ); which were estimated from the downward-looking M3 sonar (see Figure 4.6). Suspended sediment concentration,  $C_v$ , was determined from  $\Delta\rho$  using Equation 3.30, with  $\rho_s = 2650$  kg/m<sup>3</sup> and  $\rho = 1025$  kg/m<sup>3</sup>, and is plotted versus  $A_{fr}$  (or Fr) in Figure 4.5b. The solid black line is the fractional volume concentration obtained using equation 4, and ranges from  $C_v \simeq 0.015$  for  $A_{fr} = 2$  to  $C_v \simeq 0.17$  for  $A_{fr} = 0.6$ . The values of  $C_v$  from Equation 3.5 are similar, 27 % lower, indicating that these estimates are more sensitive to the choice for  $A_{fr}$  than the choice of  $h$  or  $h_0$ , in this case. While the head speed measurements indicate a decreasing trend—about 10 to 20 %—there is a lot of scatter among the estimates, and hence broad confidence bounds. Thus, for the purposes of this thesis, head speed is taken as the mean value, and is presented in Table 4.1 for the most intense measured events.

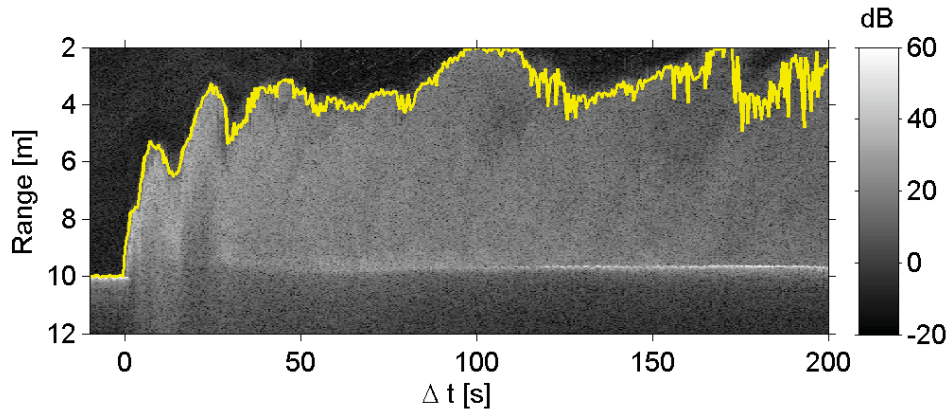


Figure 4.6: Downward-looking M3 backscatter. Intensities indicate dB (arbitrary reference). The yellow line is the estimated upper boundary of the current. Event 172C.

*Simpson* (1997) collected the empirical evidence then available for the relationship between  $Fr$  for gravity currents and water depth, mixing and friction, none of which are explicitly accounted for in Equation 3.5. For gravity currents on a flat bottom fed from a constant source under the influence of mixing and friction, and a relative water depth similar to the field site, a reasonable choice for  $Fr$  is 1.5, giving  $C_v \simeq 0.03$  (Figure 4.5). However, at the field site the bottom slope is  $\Theta \simeq 4.7^\circ$ . The *Britter and Linden* (1980) lab experiments indicate that mixing in the body increases with bottom slope, altering the profile of the current so that the head is no longer thicker than the body (see Figure 4.7). The profile of current 172C (Figure 4.6) qualitatively resembles that of the lab current on a  $5^\circ$  incline.

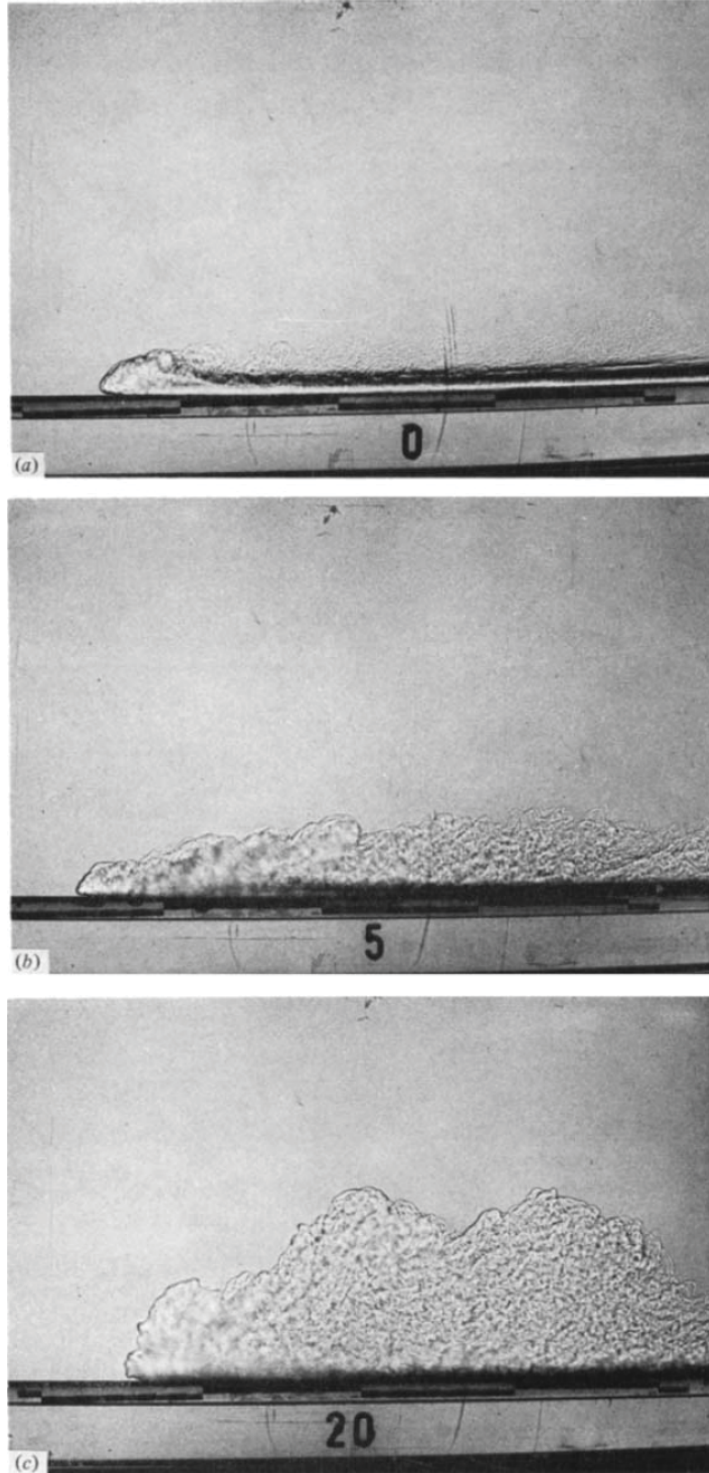


Figure 4.7: Shadowgraphs by *Britter and Linden* (1980) of saline gravity currents flowing down inclines of (a)  $0^\circ$ , (b)  $5^\circ$  and, (c)  $20^\circ$ .  $\frac{\Delta\rho}{\rho} \simeq 0.1$  and  $Q \simeq 2.5 \times 10^{-4} \text{ m}^2/\text{s}$ . (image source: *Britter and Linden* (1980))

Head heights and average body thicknesses were estimated from the downward-looking M3 sonar. Head heights were taken as the first local maximum value of the upper boundary of the current (e.g. Figure 4.6) within the time  $\Delta t = 0$  to 10 s. Average body thicknesses were taken as the average value of the upper boundary of the current in the time interval  $\Delta t = 10$  to 120 s. These values are listed in Table 4.1 for the 5 most intense events.

Event	$U_0$ [m/s]	Width [m]	$h_0$ [m]	$h$ [m]
170C	$1.74 \pm 0.17$	52	2.17	3.97
172A	$1.68 \pm 0.12$	32	2.44	3.86
172B	$2.87 \pm 0.20$	22	1.80	3.69
172C	$2.39 \pm 0.13$	82	4.68	6.39
172E	$2.07 \pm 0.14$	31	1.12	3.55

Table 4.1: Turbidity current properties from the M3 sonar imagery. The  $U_0$  values are the mean  $\pm$  the standard error.

Current widths were also estimated from the forward-looking M3 imagery. When the nose of the current reached range  $\simeq 30$  m the widest part of the current was chosen in the ranges 30 to 60 m to be the current width. This was done in order to try to measure an accurate width of the body of the current as opposed to the v shaped head, which was a common feature among most observed currents.

## 4.4 Body and Tail Properties

Velocity data from the ADCP for event 172C are presented in Figure 4.8. The bottom is at approximately 10 m range, and velocities beyond this are not real. The dark blue colors indicate NaNs: i.e. range cells for which the velocity estimates did not satisfy the ADCP error criteria. As expected the magnitude of the down-channel component is much greater than the transverse component, and reaches a maximum of roughly 2.5 m/s. The head is taken from time  $\Delta t = 0$  to 10 s, the body 10 to 120 s, and the tail 120 s onward. Down-channel velocities are stronger in the head and body of the current, and decrease in the tail. Turbulent fluctuations—of smaller magnitude than the down-channel velocities—are evident in the cross-channel velocities, and persist well after the head has passed.

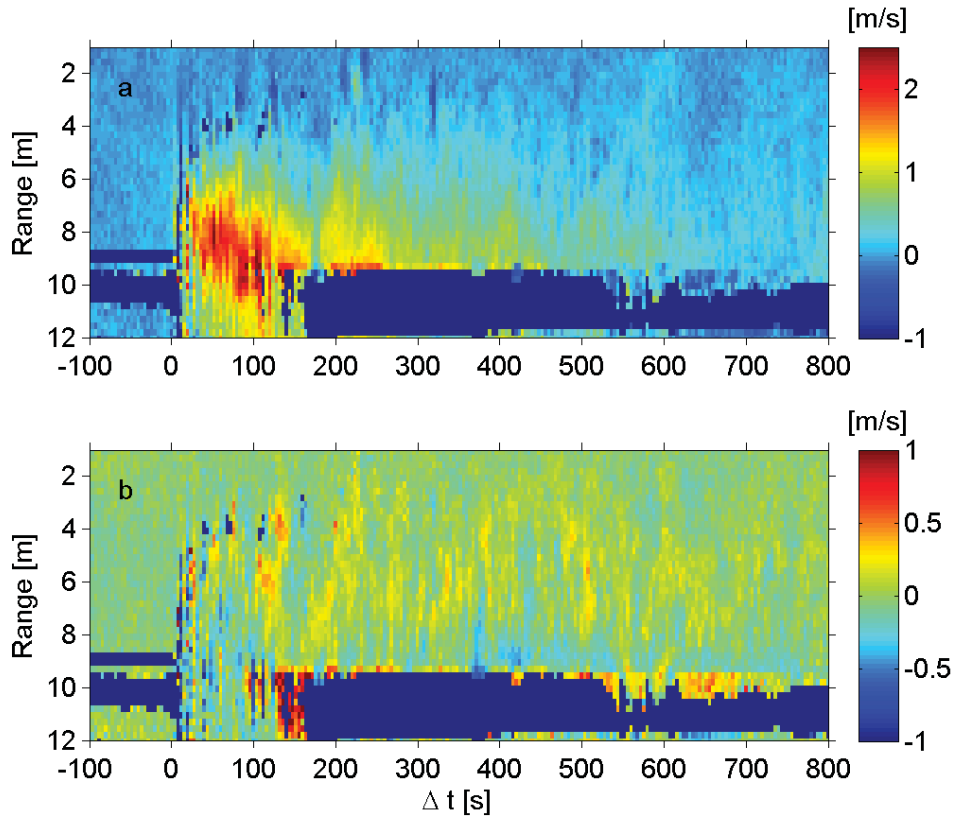


Figure 4.8: ADCP velocities: (a) down-channel component and, (b) cross-channel component. Event 172C.

It is evident from Figure 4.8 that sustained flow speeds greater than 0.5 m/s were confined to heights less than 5 m above bottom. However, for relatively strong currents such as 172C, the instrument attitude was affected by turbulent eddies reaching the height of the instrument frame (Figure 4.9).

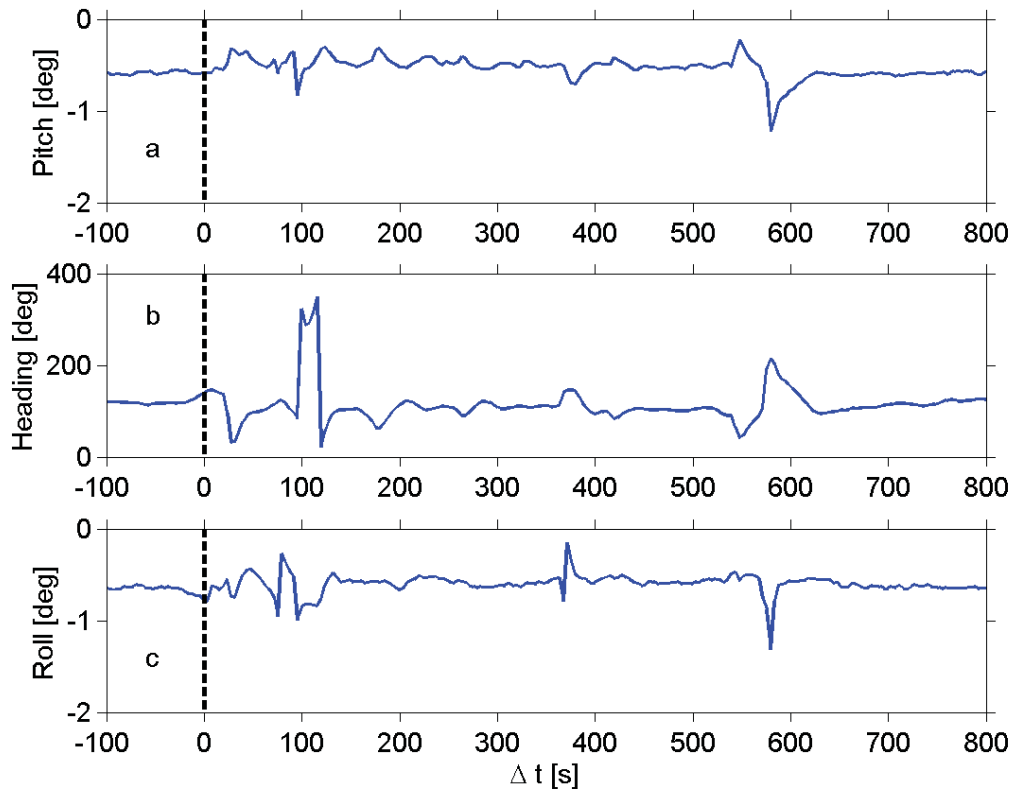


Figure 4.9: ADCP attitude: (a) pitch, (b) heading, and (c) roll. Event 172C.

Figure 4.10 shows velocities at about 1 m above the bottom, as measured by the ADCP. The average frontal speed measured by the forward looking M3 is indicated by the red stars, and red best-fit line in Figure 4.10a. Maximum flow speeds measured within the current by the ADCP compare well with the M3 derived turbidity current frontal speeds. The peak down-channel velocities measured by the ADCP lag the turbidity current arrival time beneath the M3 frame by about 40 s, due to the ADCP's location roughly 30 m farther down channel. The frontal speed of the current as measured by the M3 indicates a slight decelerating trend, as mentioned previously. (Note that the ADCP, because of the diverging beam geometry, does not provide a representative measurement of head speed.)

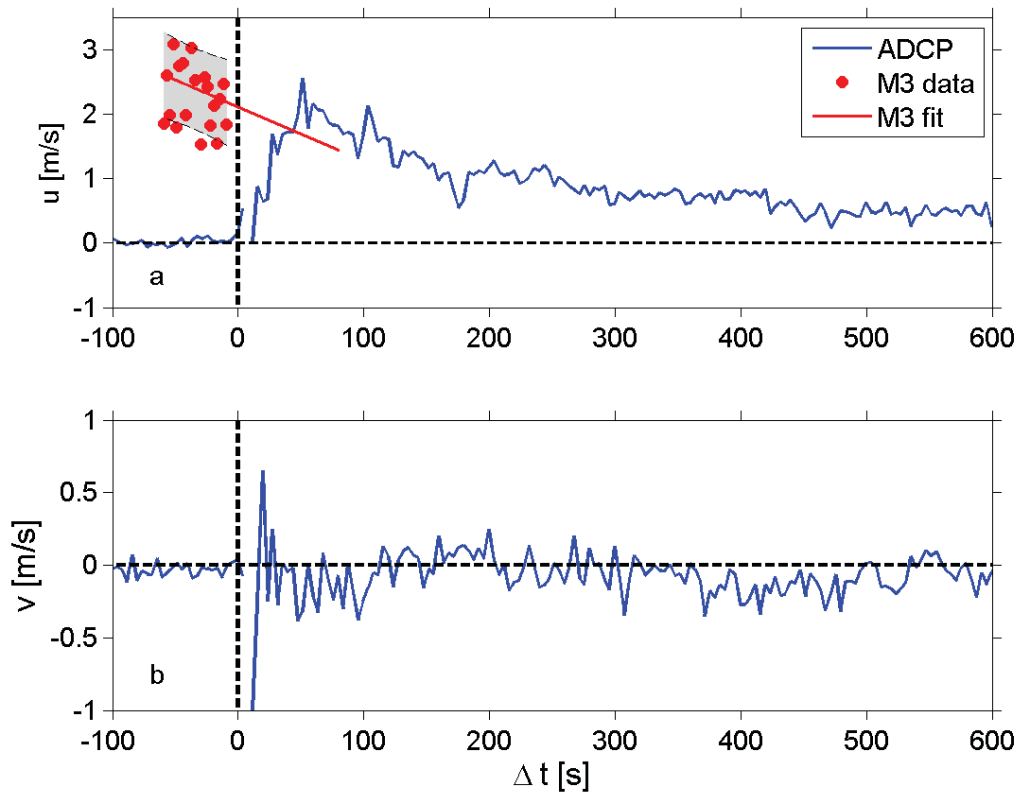


Figure 4.10: ADCP velocities at 1 m above the bottom and frontal velocities determined from the M3 imagery: (a) down-channel velocities and, (b) cross-channel velocities. The red line is the least-squares best fit to the M3 data extrapolated forward in time. The grey shading is the 90 % confidence interval of the fit. Event 172C.

Figure 4.11a shows the turbidity current thickness,  $h$ , estimated from the downward-looking M3. Using this thickness, the ADCP down-channel velocities in Figure 4.10a, and  $C_d = 5 \times 10^{-3}$ , Equation 3.2 yields the  $C_v$  estimates in Figure 4.11c. This method of estimating suspended sediment concentration gives maximum values of roughly  $C_v = 0.003$ , an order of magnitude smaller than the estimates based on frontal speed in Figure 4.5b. This is qualitatively expected, due to this method of estimating suspended sediment concentration being more indicative of overall body concentration values.

The along-channel velocities measured by the ADCP (Figure 4.8a) were integrated vertically to obtain an estimate of  $Q$  (volume flux per unit width), shown in Figure 4.11b. This was used for the time period of constant  $Q$  associated with the body of the current ( $\Delta t = 40$  to  $100$  s), along with head velocity  $U_0 = 2.1$  m/s (interpolated to  $\Delta t = 0$ ), to

obtain an estimate of  $C_v \simeq 0.03$  for the current, from Equation 3.7. This is plotted in Figure 4.11d as the solid red line. The dashed black lines indicate  $U_0/(g'Q)^{1/3} = 1.3$  and 1.7. This is in good agreement with the  $C_v$  estimated from the head speed of a current on a flat bottom with  $Fr \simeq 1.5$  (see Figure 4.5b).

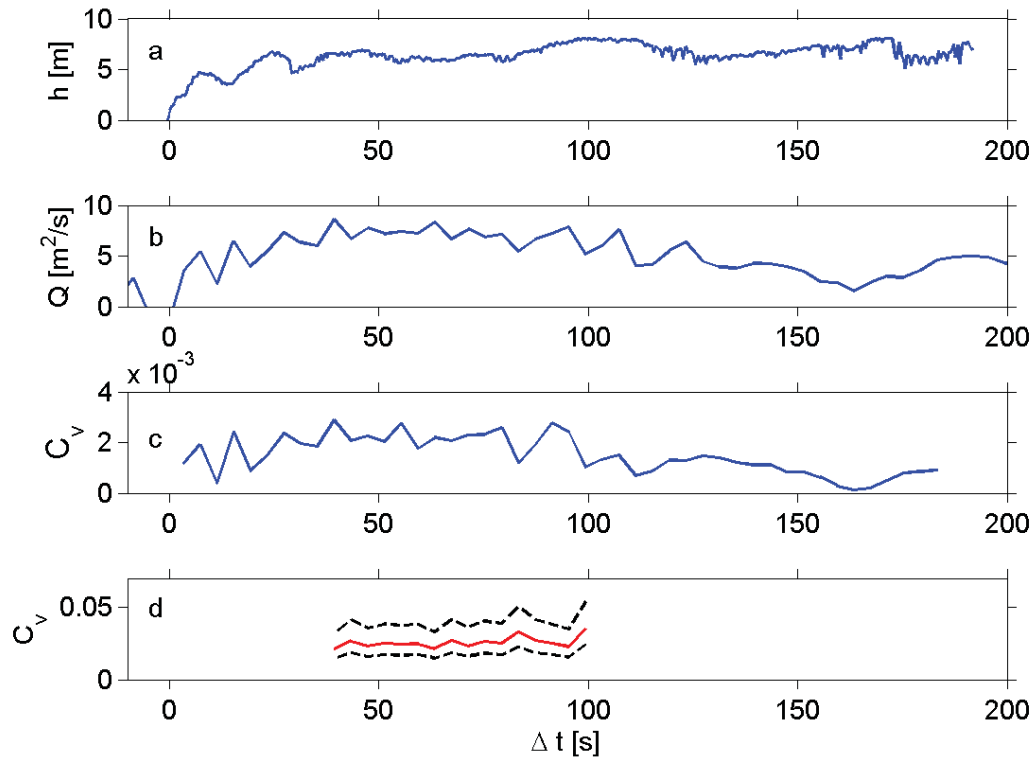


Figure 4.11: (a) Turbidity current thickness,  $h$ , from the downward-looking M3, (b) volume flux per width,  $Q$ , from the ADCP data, suspended sediment concentration estimated from: (c) Equation 3.2 with  $C_d = 5 \times 10^{-3}$ ; and (d) Equation 3.7. Event 172C.

## 4.5 Suspended Sediment Concentration from Acoustic Backscatter

As outlined in Section 3.4.4, the intensity of backscatter versus range for two different frequencies can be used to estimate sediment concentration. This approach was implemented for data from the downward-directed 500 kHz M3 center beam, and the 200 kHz Knudsen single beam data. Figure 4.12c corresponds to the right hand side of Equation

3.35,  $\chi$ , plotted against  $z_A - z_B$ ,  $z_A$  is chosen to be at range = 2 m.  $\chi$  is plotted in Figure 4.13 for the time intervals  $\Delta t = 8$  to 14 s,  $\Delta t = 20$  to 26 s, and  $\Delta t = 60$  to 66 s. A linear fit is shown for the region inside the current, for the given time periods. Figure 4.14 shows values for the left hand side of Equation 3.37, for various values of particle diameter and sediment concentration. Using the slopes from Figure 4.13, and the D50 for the Squamish sample ( $163 \mu\text{m}$ ), gives an estimate of sediment concentration  $C_v \simeq 0.041$ ,  $0.036$  and  $0.005$  at  $\Delta t \simeq 11$ ,  $23$  and  $63$  s, respectively. This is in relatively good agreement with prior estimates of suspended sediment concentration, within the head and body of the turbidity current.

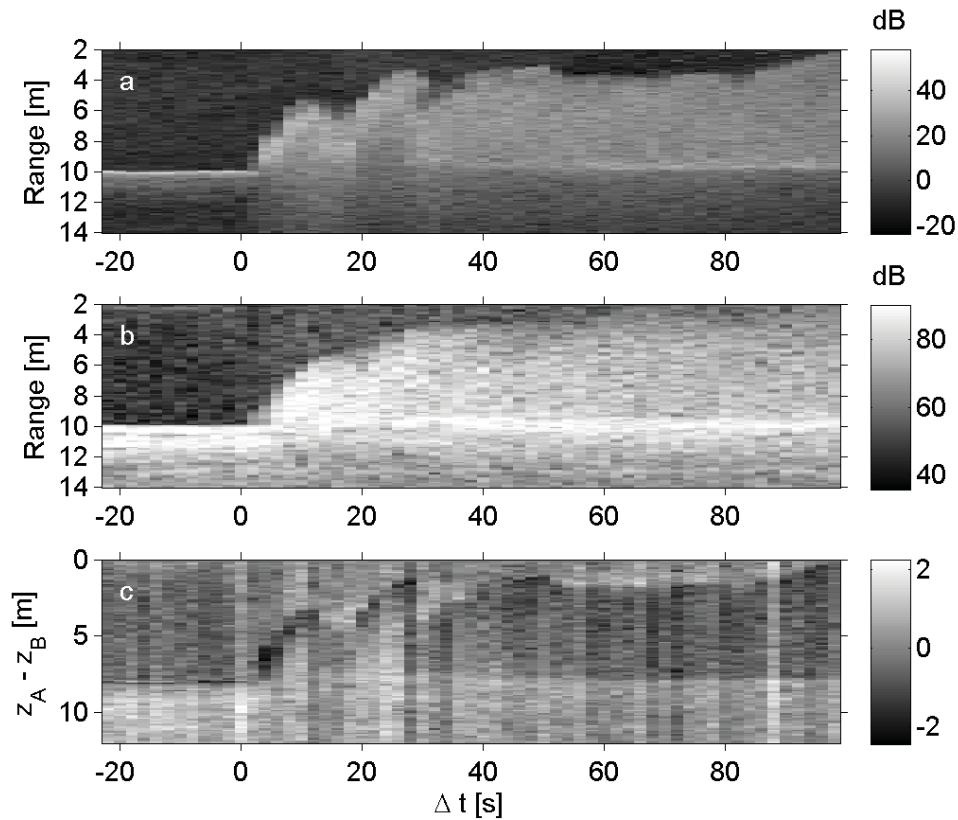


Figure 4.12: Backscatter intensity from: (a) the M3 (500 kHz); and (b) the Knudsen (200 kHz). The grayscale indicates dB (arbitrary reference).  $\chi$ , the right hand side of Equation 3.37, is plotted in (c). Event 172C.

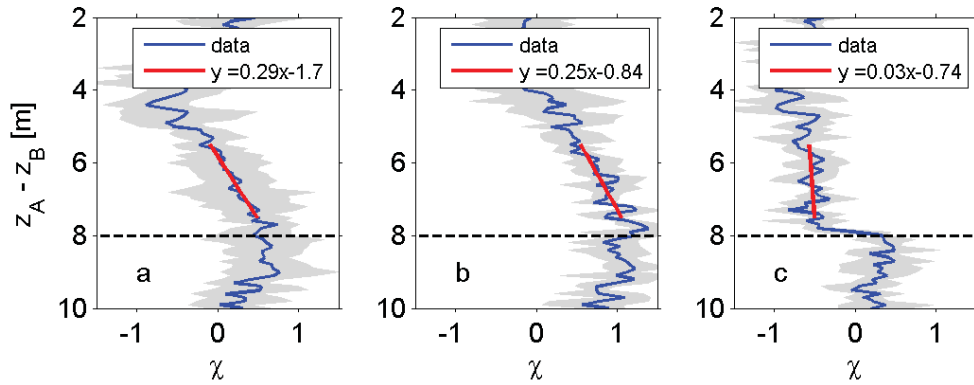


Figure 4.13:  $\chi$ , right hand side of Equation 3.37 vs.  $z_A - z_B$  for time intervals: (a)  $\Delta t = 8$  to 14 s, (b)  $\Delta t = 20$  to 26 s and, (c)  $\Delta t = 60$  to 66 s. The red lines are least-squares best fits for the range interval  $z_A - z_B = 5.5$  to 7.5 m. The shading indicates  $\pm$  the standard deviation of the data. Dashed black lines at  $z_A - z_B = 8$  indicate the bottom. Event 172C.

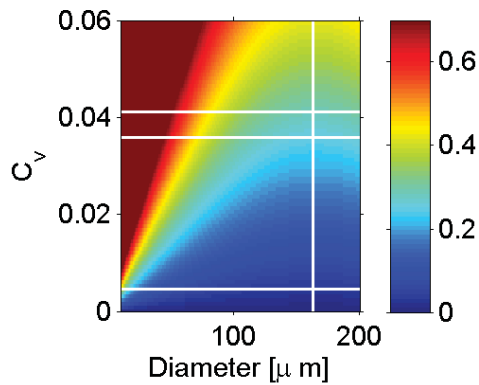


Figure 4.14: Values of  $n(\Sigma_{T_1} - \Sigma_{T_2})$  (in colour) as a function of grain diameter and concentration. The vertical white line indicates the sample D50 ( $163 \mu\text{m}$ ) and the horizontal white lines indicate the suspended sediment concentrations at the values of  $n(\Sigma_{T_1} - \Sigma_{T_2})$  equal to the slopes of the best-fit lines in Figure 4.13.

---

## CHAPTER 5

---

# MEASURED AND PREDICTED NOISE FROM TURBIDITY CURRENTS

This chapter addresses the following: (i) the characteristics of the noise produced by the Howe Sound turbidity currents; (ii) is this noise consistent with the SGN theory? The passive acoustic measurements are presented first, and a power law relationship between turbidity current head speed and sound pressure level is inferred. It is shown that the exponent in this power law can be explained by SGN theory, and that the predicted spectra—both magnitude and shape—are comparable to the measurements.

## 5.1 Observations

### 5.1.1 Event Detection

The spectrogram computed from the hydrophone data, and the acoustic backscatter from the center beam of the downward-looking M3 are shown in Figure 5.1, for event 172C.

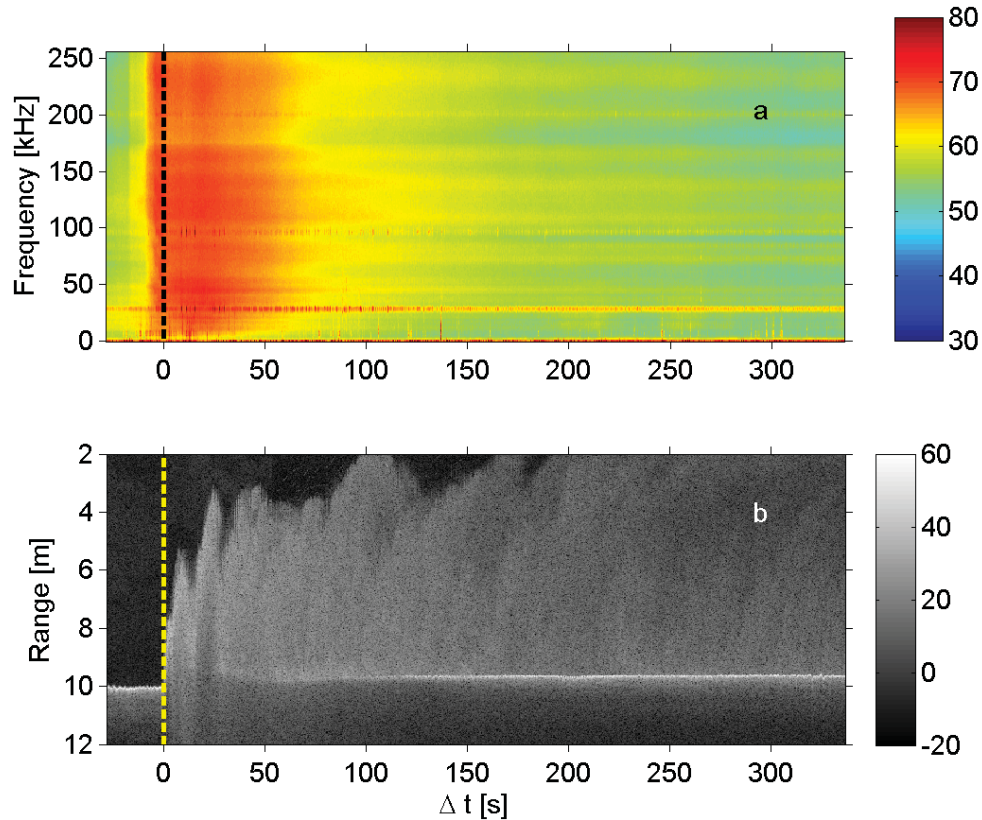


Figure 5.1: Turbidity current 172C. (a) Noise spectrogram. Colours indicate dB re  $1 \mu\text{Pa}/(\text{Hz})^{1/2}$ . (b) Acoustic backscatter at 500 kHz from the centre beam of the downward-looking M3 sonar, grayscale indicates dB (arbitrary reference). The dashed lines denote the turbidity current arrival time.

An abrupt increase in the ambient noise level, preceding the turbidity current front arrival by about 10 s, is followed by a prolonged falling off of the noise level once the front has passed. Beneath the head of the current, the bottom return in the M3 backscatter data disappeared. As shown earlier, this is most likely due to attenuation of the 500 kHz signal by the high concentration of suspended sediment in the head of the turbidity current. Also, after the current head had passed, and concentrations of sediment in the water had declined sufficiently for the bottom return to reappear, the bed was roughly 10 – 20 cm higher, indicating appreciable sediment deposition in the area directly beneath the frame. This is associated with cyclic step migration (*Hughes Clarke (2016)*).

Further evidence of very broadband noise, produced by the turbidity current, can be seen in both the single-beam sounder data (Figure 4.1), and the EM710 multi-beam data (Figure

4.2). Coincident with the initial arrival of the turbidity current, at roughly 16:49, increased signal levels of nearly equal intensity are evident at all depths, both above and below the bottom, lasting for roughly 1 min. These higher signal levels – across the frequency band spanned by the three sonars : i.e. 28, 70-100, and 200 kHz – persisted for roughly the same time as the noise from turbidity current 172C detected by the hydrophone.

Figure 5.2 is a spectrogram computed from the hydrophone data spanning roughly four hours centred around lower low water on Yearday 172. The dashed vertical lines indicate the arrival times of the leading edge of turbidity currents detected by the downward-looking M3 sonar. These arrival times frequently coincide with pronounced increases in broadband noise, especially for the higher amplitude (i.e. louder) events: B, C and E. The quieter events (A,D,F and G) are in some cases not coincident with the M3 arrival times, and the possible reasons for this are discussed later. First, the focus is on the louder events, which do coincide with M3 arrival times.

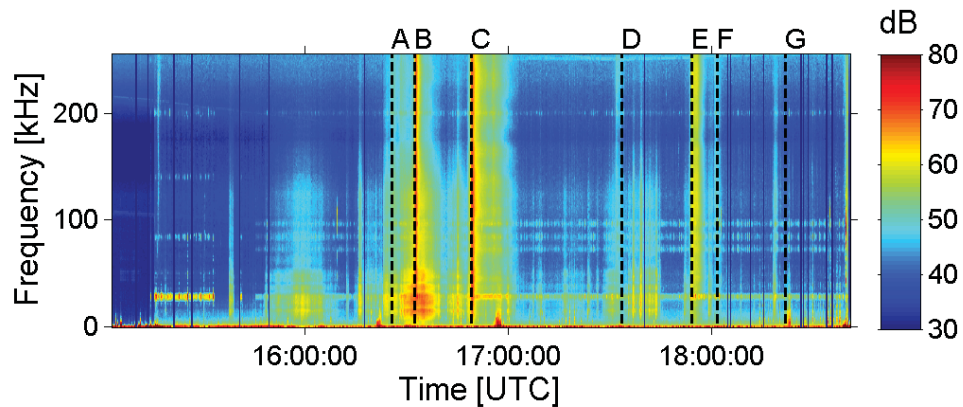


Figure 5.2: Ambient noise spectrogram for YD 172, with dashed black lines indicating turbidity current arrival times from the M3 multi-beam sonar. Solid dark blue lines are periods of time lacking spectral data. Colours indicate dB re  $1 \mu\text{Pa}/(\text{Hz})^{1/2}$ .

### 5.1.2 The Louder Events

Events 170C, 172A, 172B, 172C and 172E were the five loudest events observed and are focussed on. Spectrograms spanning about 4 min centred on the turbidity current arrival times are shown in Figure 5.3 for four of the louder events. Average frontal head speeds and approximate current widths as calculated from the M3 forward looking sonar (see section 4.3) are listed in Table 4.1 and velocities ranged from roughly 2.8 m/s for 172B to

1.9 m/s for 172A, widths ranged from 22 m for 172B to 82 m for 172C. These data reveal some commonalities among events. All events exhibit broad band noise associated with the currents ranging from about 10 kHz to the upper limit of detection of the instrument, about 250 kHz. In all cases signal levels over this broad frequency range appear to reach levels close to their maximum roughly 10 s before the turbidity current arrival times in all cases. Pronounced temporal asymmetry is observed in all four cases: that is, the sound levels increase abruptly across all frequencies as the turbidity current approaches the instrument, and fall off gradually after the passage of the head.

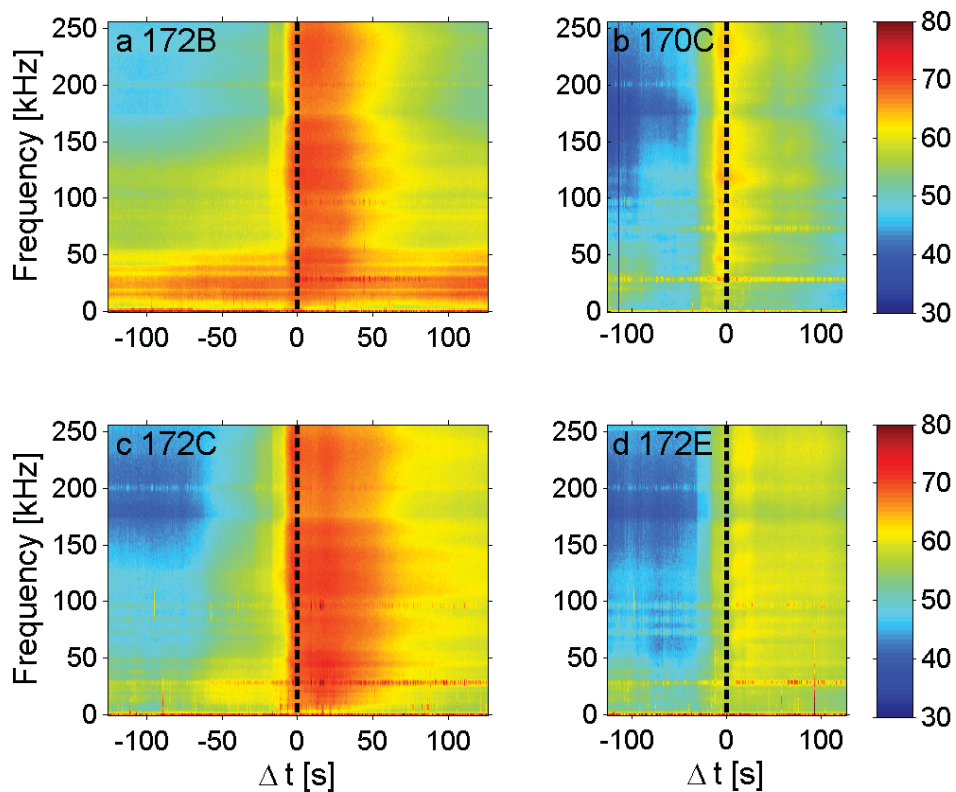


Figure 5.3: Spectrograms of turbidity current event noise, each spanning roughly 4 minutes. The colour scales are the same for the four panels, and represent dB re  $1 \mu\text{Pa}/(\text{Hz})^{1/2}$ . The associated turbidity current M3 derived frontal speeds and widths are listed in Table 4.1.

The duration of time for which noise associated with a turbidity current was detectable by the hydrophone was qualitatively estimated from the spectrograms for these five events. These durations were found to be about 6 min on average, with a maximum of about 13 min for event 172C, and a minimum of about 2 min for event 172A.

### 5.1.3 Turbidity Current Noise Spectra

Figure 5.4 shows ambient noise spectra for all turbidity currents in Table 4.1, as well as the minimum ambient noise spectrum for Yearday 172. Each spectrum is an average over a 1 s interval centred on the event arrival time.

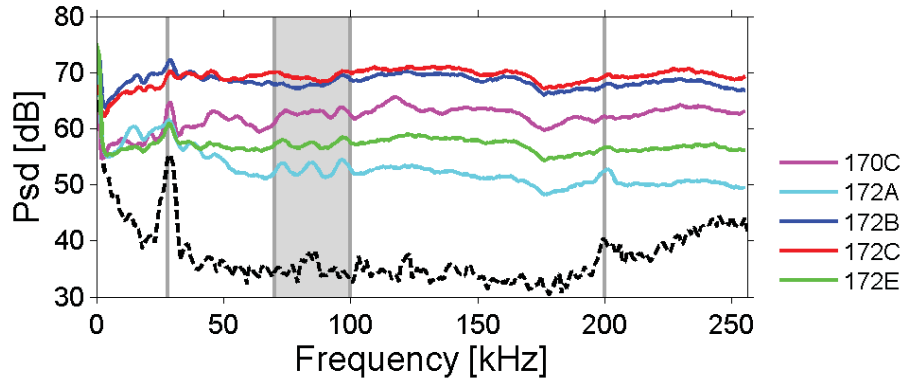


Figure 5.4: Turbidity current noise spectra for the louder events as the head passed directly beneath the hydrophone. The dashed black line is the minimum ambient noise spectrum for the recording period on YD 172. The values are in dB re  $1 \mu\text{Pa}/(\text{Hz})^{1/2}$ . Grey shading indicates bands of active sonar noise.

The minimum ambient noise spectrum (dashed black line) was taken when the total energy level (the integral of the spectra over frequency), for a 1 s interval, was a minimum for the duration of the instruments submerged period on YD 172.

Evidence of active sonar noise that was not completely removed in the data processing stage is still evident at 28, 70 – 100 (three peaks), and 200 kHz (highlighted in grey in Figure 5.4). The dip at roughly 175 kHz is due to the hydrophone transducer resonance at this frequency, and the supplied instrument response curve (applied as a calibration) over-correcting for it. This resonance is evident in the uncalibrated data (see Figure 2.3b).

The spectral shapes show relatively little difference for all events and are all relatively flat, especially above 50 kHz. For frequencies from 50 to 200 kHz, the spectra are roughly 10 to 30 dB above ambient.

### 5.1.4 Sound Intensity vs. Head Speed

Mean sound pressure squared, in the frequency range 130 kHz to 150 kHz, divided by current width, is plotted as a function of turbidity current head speed in Figure 5.5; in

log-log form. The data are well-represented by a straight line, indicating a power-law dependence of sound intensity on head speed,  $U_0^m$ . The best-fit value for the exponent  $m$  is 7.1 (solid black line in Figure 5.5). Note however, that the 90 % confidence interval on this fit value of  $\pm 5.1$ , is quite wide. The p-value associated with the fit is 0.04. The standard errors associated with the head speed estimates are plotted as horizontal error bars. RMS error estimates associated with the spectral estimates of  $P^2$  are shown as vertical error bars. Estimates of the error associated with the turbidity current width measurements would further increase the vertical error bars, but are not included in this analysis.

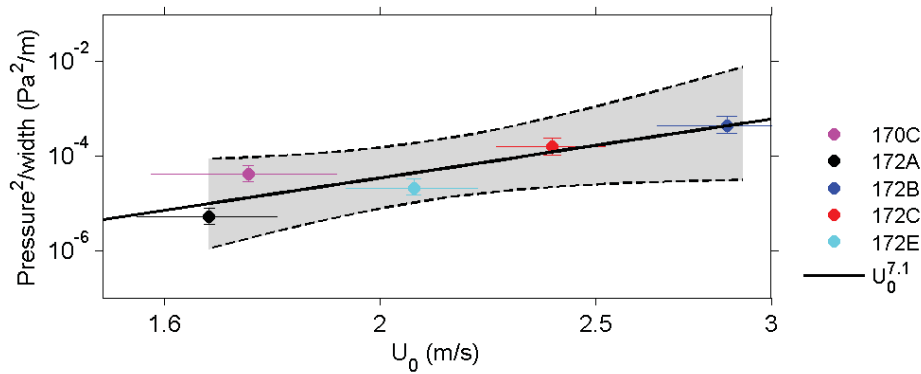


Figure 5.5: Mean pressure squared, normalized by current width, in the 130 to 150 kHz frequency band as a function of head speed. The points indicate measurements from the 5 loudest turbidity currents, with the horizontal and vertical lines indicating the standard errors associated with the measurements. The solid black line is a power law fit to the data, and the dashed blacked lines (and grey shading) indicate the 90% confidence intervals related to the fit.

The theory suggests that sound pressure per collision is proportional to collision speed (Equation 3.15), which is proportional to shear stress ( $u_*$ ), and therefore to  $U_0$ . Since sound intensity is proportional to pressure squared it follows that sound intensity should be proportional to  $U_0^2$ . Assuming Equation 3.17 holds, the number of collisions per unit time is proportional to  $C_v^2$  and  $U_c$  (which is proportional to  $U_0$ ). The concentration,  $C_v$ , is proportional to velocity-squared (Equation 3.5), so the number of collisions per unit time is expected to be proportional to  $U_0^5$ , giving intensity proportional to  $U_0^7$ . This matches well the power law fit to data of  $U_0^{7.1}$ .

## 5.2 Propagation Effects

### 5.2.1 Turbidity Current SGN Asymmetry

The temporal asymmetry seen in the SGN for the more intense currents is illustrated again in Figure 5.6a. For comparison a simple 1-D model taking into account only seawater absorption (*Fisher and Simmons (1977)*) as a function of straight line distance to the receiver is shown figure 5.6b. The source is assumed to be the measured spectrum at  $\Delta t = 0$ . The current is assumed to be an omni-directional point source moving at a constant speed of 2.47 m/s.

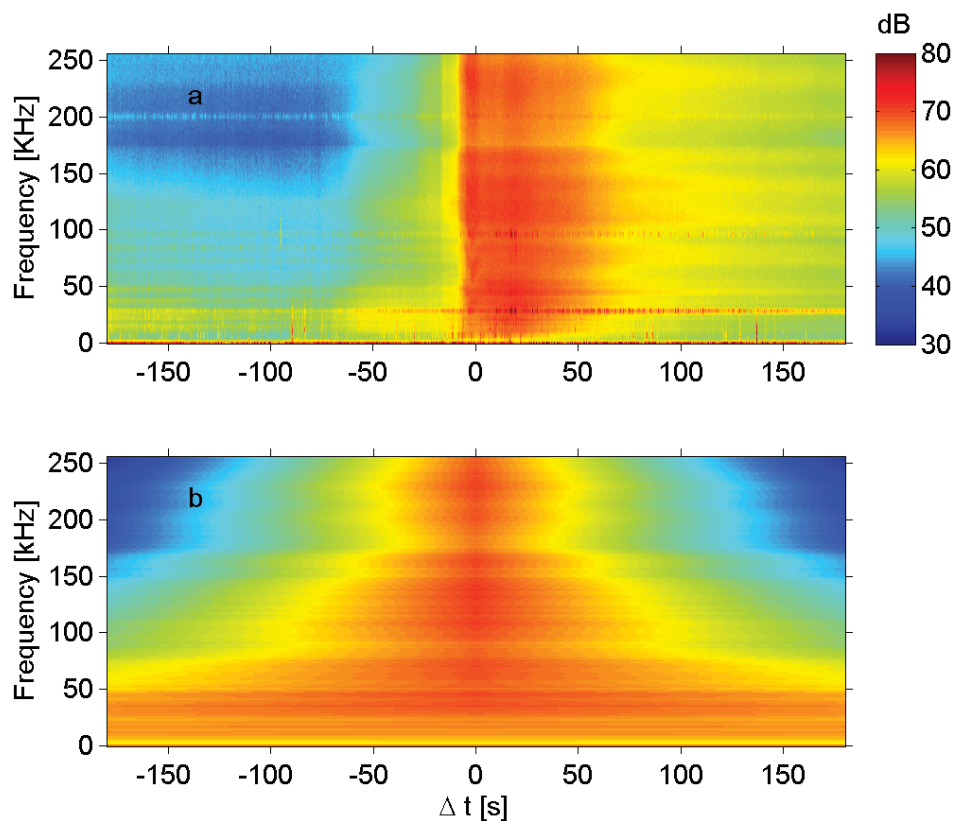


Figure 5.6: (a) Measured turbidity current noise, and (b) estimated received signal with straight-line seawater absorption. The colourscale represents dB re  $1 \mu\text{Pa}/(\text{Hz})^{1/2}$ . Event 172C.

The simple model qualitatively captures the continuous reduction with time of the sound intensity after the turbidity current front has passed, at frequencies greater than about 100 kHz. This is not true for sound preceding the arrival of the front: i.e. the simple model

serves to emphasize the pronounced temporal asymmetry in the observed spectrogram. Thus, either the source is highly directional and/or more complex sound propagation effects are at play.

### 5.2.2 2-D Ray Tracing Model

In order to determine whether the temporal asymmetry in the measured SGN might be due to source-to-receiver propagation effects (e.g. refraction), a ray trace model, BELLHOP, was used. BELLHOP numerically solves the ray equations (Section 3.4.1) and estimates transmission loss.

Figure 5.7 is a plot of measured sound speed profiles in the vicinity of the delta slope. The black line was from a single cast of the AML sound velocity instrument. The blue line is from an independent measurement from the  $\mu$ CTD. The AML sound speed profile was used in the model.

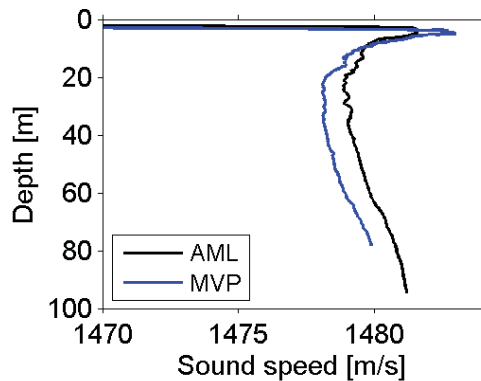


Figure 5.7: Field site sound speed profiles from the AML Sound Velocity instrument and the AML  $\mu$ CTD instrument.

The profiles are characterized by much slower sound speeds in the first few meters, due to the lens of freshwater river run-off, and a sound speed minimum at about 30 m depth. The presence of the minimum suggests that (some of) the sound energy from a source moving from shallow to deep water might be trapped in a mid-depth sound duct.

Using the sound speed profile, a simple linearly sloped ( $8.5^\circ$ ) bathymetry, with slope similar to the delta in Howe Sound, and an omni-directional source (0.5 m above the bottom at depth 60 m), transmission loss was modelled in the domain. The predicted losses for a 20 and 200 kHz point source are shown in Figure 5.8.

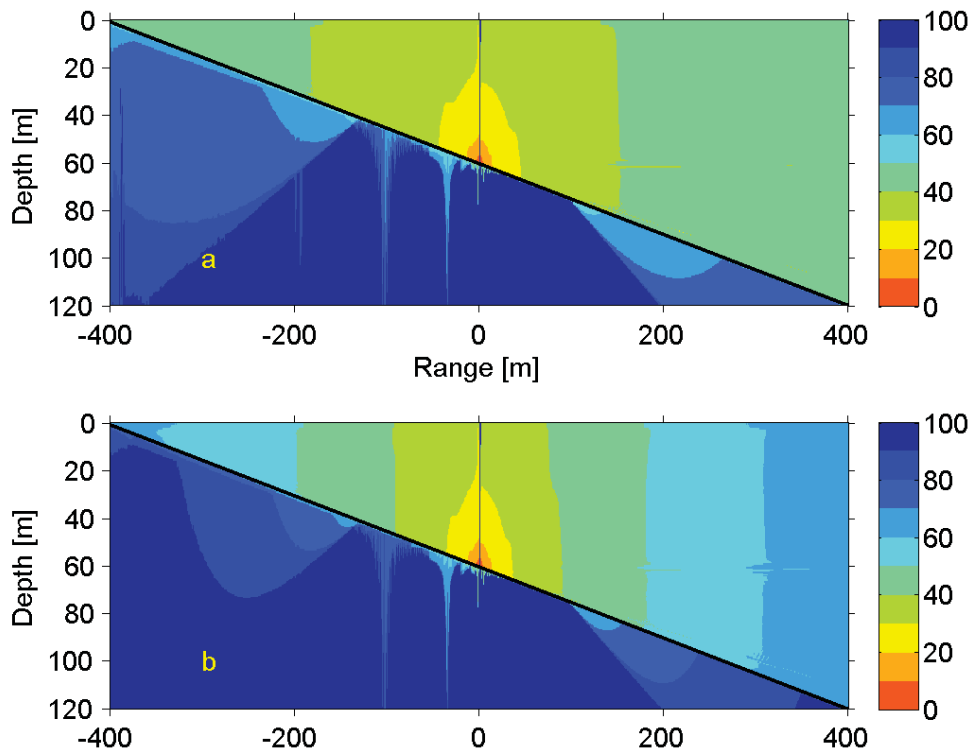


Figure 5.8: BELLHOP modelled transmission loss for an omni-directional point source on a linearly sloped bathymetry: (a) 20 kHz and (b) 200 kHz. The colors indicate dB of transmission loss.

As expected, 200 kHz sound is attenuated more strongly than 20 kHz. However, these model results do not exhibit pronounced up- and down-slope differences in the immediate vicinity of the source, thus indicating that neither water column refraction, nor seabed absorption are likely contributors to the observed asymmetry seen in the received SGN signal.

### 5.2.3 Hydrophone Listening Radius

For a single receiver—suspended above the bottom, and assuming only straight line paths—there will be an area of seafloor (beneath the hydrophone) outside of which signals produced on the bottom will be so severely attenuated (during propagation to the receiver) so as to be insignificant to the total received signal. In this context, the radius—which defines an area of sea-floor—for which this is true is defined as the hydrophone listening

radius. For a given slant angle to the hydrophone, and hence slant range, the sound from a near bottom source propagating along that slant range will undergo spreading, and frequency dependent scattering and attenuation along that path.

The source region is treated as an infinite sheet sound source emanating from the bottom (Figure 3.5). Using Equation 3.33, the Squamish grainsize distribution,  $z_h = 10$  m and  $z_s = 4.7$  m (i.e. the head height of current 172C), sound pressure levels for a given patch radii, and sediment concentrations were computed for 200 kHz, and are shown in Figure 5.9a. The listening radius was taken to be the value of  $r$  at which the sound pressure reached 95% of its asymptotic value. The listening radius as a function of concentration is shown in Figure 5.9b.

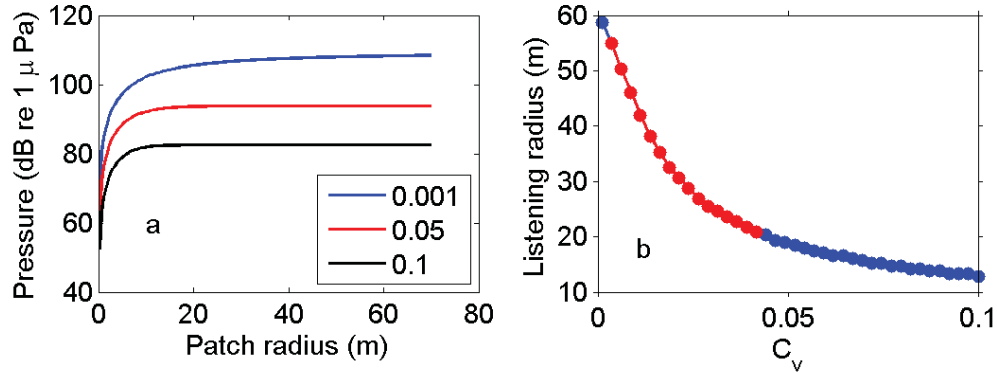


Figure 5.9: Listening radius at 200 kHz: (a) sound pressure levels as a function patch radius for various sediment concentrations and, (b) Listening radius as a function of sediment concentration. The range of estimated values of  $C_v$  are indicated in red. Event 172C.

## 5.2.4 Time Dependence of Sound Emitting Patch

The appropriate choice of the integration limits in Equation 3.33 allows the calculations to be done when a fraction of the listening area is emitting sound. If a current is assumed to travel through the listening area, and only the parts of the listening area covered by the current are assumed to emit sound, then the choice of these limits allows a time dependent calculation of received sound. Figure 5.10 shows the integral taken in this way at sequential time steps, using conditions similar to event 172C. Head speed was chosen as  $U_0 = 2.47$  m/s,  $C_v = 0.03$ ,  $z_s = 4.7$  m,  $z_h = 10$  m, and sound emitting patch radius  $r_p = 50$  m (larger than the listening radius of roughly 30 m, at 200 kHz, for this concentration). The

source pressure squared per area of bottom was arbitrarily chosen as  $P_0^2 = 0.1 \text{ Pa}^2/\text{m}^2$ , so that the sound pressure levels received, when the whole patch was emitting sound, were roughly equivalent to the sound pressure levels of the data for  $\Delta t = 0$  to 20 s.

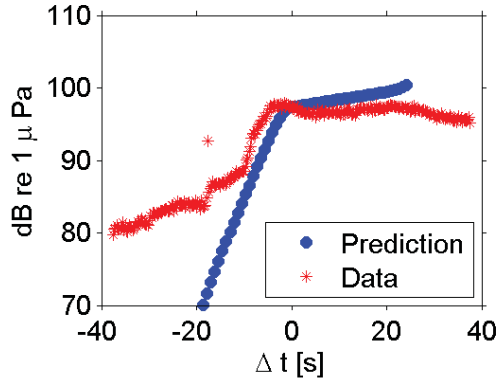


Figure 5.10: Predicted arrival time vs. measurements at 180 kHz. Event 172C.

The arrival times, at roughly 10 seconds preceding the current, are nearly coincident for both the simple model and the data. This indicates that the hydrophone is only detecting the sound when the current has entered the listening area, that is, sound is unable to be projected forward of the current. If the situation was the same as the current moved out of the listening area, then a similar fall-off would be expected. This is not seen in the data. Two factors are speculated to be at play in causing this: (1) the current continues to produce SGN in its body, after the head has passed, with decreasing collision velocities and collision occurrences causing decreased source pressure levels; and (2) a considerably reduced sediment concentration in the body and tail of the current, allowing sound produced at, or near, the head to be projected backward, and perhaps sideways. Regarding the inability of sound to be projected forward, it is likely due either to very high sediment concentrations in the nose of the current, and/or bubbles released from the sediment acting as a sound absorbing screen within the nose.

### 5.3 Comparison to Theory

The frequency  $f_t = 1/2t_0$ , indicative of the peak in the SGN spectrum, for the sound produced by collisions among particles of a given size, can be calculated using Equation

3.14. Choosing  $E = 4.6 \times 10^{10} \text{ kgm}^{-1}\text{s}^{-2}$ ,  $\rho_s = 2650 \text{ kg/m}^3$ ,  $\sigma = 0.3$ ,  $2a = 163 \text{ }\mu\text{m}$  (the D50 of the field sample), and  $U_c = 0.94 \text{ m/s}$  for Event 172C, a frequency  $f_t \approx 850 \text{ kHz}$  is obtained. This is well above the 256 kHz maximum frequency detectable by the hydrophone. However, as discussed in Chapter 3, it is expected that the sound generated by the turbidity current is from the near bottom, high concentration layer, and that this layer would be comprised of particles from the larger size classes. For example, the same calculation done with the sample D90 (491  $\mu\text{m}$ ) gives  $f_t \approx 281 \text{ kHz}$ . Considering also that the SGN spectra obtained by *Thorne* (1985) in his experiments extended to frequencies well below  $f_t$ , these calculations point to SGN being the probable cause of the measured sound from turbidity currents. This possibility is pursued in the following section.

### 5.3.1 Predicted SGN Spectra

To gain insight into the shape of the SGN spectrum, the distribution of particle size must be taken into account. Due to differential settling speeds as a function of particle size, it is likely in a turbulent flow like a turbidity current that larger particles will be concentrated near the bed, as has been demonstrated experimentally in lab studies (e.g. *Sequeiros et al.* (2009)). The Vanoni distribution (Section 3.1.2) defines concentration profiles for particles of different size classes, with more of the larger particles being nearer the bottom of the current. For this thesis a simplified approach is used whereby the size distribution is divided into two groups: (1) smaller particles which are assumed to remain in suspension within the turbulent interior of the flow, and (2) larger particles which are assumed to be confined to the higher concentration nearbed region, and are thus involved in the collision process. The choice of the diameter separating the size distribution into “large” and “small” influences both the shape and magnitude of the predicted SGN spectra, because it defines the size distribution within the bedload layer and hence both the size and numbers of colliding particles. The choice also affects propagation losses through the turbid interior because it defines the size distribution of particles in suspension.

The model geometry is illustrated in Figure 3.5. For the sound producing nearbed layer,  $z_{bl}$ , the number of collisions that occur per unit volume per unit time between two size classes of particles at collision speed  $U_c$  is given by  $W_{ij}$  (Equation 3.17). The theoretical spectrum for a collision between particle  $j$  and  $i$  is taken at field distance  $r_0 = z_{bl}$  and is averaged over all field angles to the collision  $\theta = 0^\circ$  to  $360^\circ$  (see Section 3.2.1). All spectra from collisions between any two particles in the total set of particle sizes are multiplied by

$W_{ij}$  and summed together. This gives a source level spectrum for the area element  $dA$ .

The spectrum of the signal at the receiver (at height  $z_h$ ) is the integration of the source pressure per area element,  $dA$ , over the listening area of the hydrophone taking into account propagation effects through the water and turbid layer as outlined in section 3.4.3. The source sound pressure is taken at a reference height  $z_0 = r_0/2$  above the top of the nearbed layer.

Two cases are considered: 1) The size distribution D50 (0.17 mm) is used as a cut-off and 2) 0.8 mm is used based on it producing the flattest (qualitative) spectrum. In the second case roughly 3% of the size distribution falls within the large particle group. The concentration in the nearbed layer  $C_{vbl}$  is chosen as 0.1 and also 0.2 for case 2 as a comparison.

Conditions similar to event 172C were chosen. The height of the receiver above the bottom  $z_h = 10$  m. The height of the turbid layer,  $z_s$ , was chosen as the head height,  $h_0 = 4.7$ . The concentration within the suspended layer,  $C_v = 0.027$ , was calculated using Equation 3.5 with  $Fr = 1.5$ , and  $h_0$ . The radius of the sound emitting patch was chosen to be 40 m, based on the width of the current being roughly 80 m, (Table 4.1) and the listening radius for this concentration at 200 kHz being roughly 30 m. The collision speed  $U_c = 0.94$  m/s was set equal to  $2u_*$  (see Equation 3.6). Values for  $u_*$ ,  $z_{bl}$ , and  $\theta_s$  are presented in Table 5.1 for the five most intense events observed.  $\theta_s$  for event 172C was about 14, indicating the assumption of a sheet flow is valid. Other values were chosen as:  $\rho_s = 2650$  kg/m<sup>3</sup>,  $\rho = 1025$  kg/m<sup>3</sup>,  $E = 4.6 \times 10^{10}$  kgm<sup>-1</sup>s<sup>-2</sup>,  $v = 0.3$ ,  $\nu = 1 \times 10^{-6}$  m<sup>2</sup>/s and  $c = 1500$  m/s.

Event	$u_*$ (m/s)	$\theta_s$	$z_{bl}$ (m)
170C	0.33	7.2	0.12
172A	0.32	6.6	0.11
172B	0.55	19.4	0.31
172C	0.46	13.5	0.22
172E	0.40	10.1	0.16

Table 5.1: Turbidity current bedload layer properties, for  $C_{vbl} = 0.1$ , with only particles larger than  $d = 0.8$  mm in the bedload layer.

Figure 5.11 shows predicted spectra at the receiver and spectral data averaged over a 1 s period centred on the arrival time of event 172C.

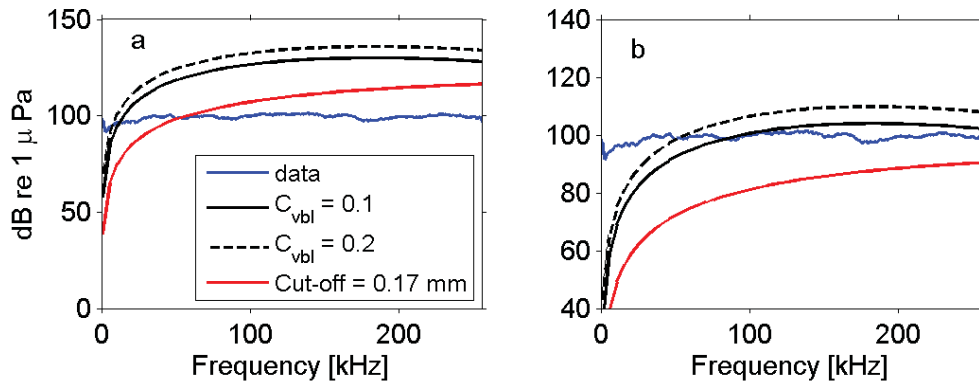


Figure 5.11: Predicted SGN spectra versus observations (blue line) for the cases when: a) all particles, and b) 5% of the particles in the nearbed layer are assumed to be involved in the collision process at an instant in time. The black lines assume a cut-off grain size of 0.8 mm and  $C_{vbl} = 0.1$  (solid line) or 0.2 (dashed line). The red line assumes a cut-off grain size of 0.17 mm and  $C_{vbl} = 0.1$ . Event 172C.

When more smaller particles are included in the bedload sound producing layer (red line) there is relatively more energy at higher frequencies, due to smaller particles producing higher peak frequencies when colliding. However, spectral levels over all frequencies are lower than when smaller particles are omitted (black lines), due to larger particle collisions producing comparatively louder noise than smaller particle collisions. Choice of a more concentrated bedload sound producing layer (dashed black line) results in overall louder spectral levels, due to a higher collision rate.

In Figure 5.11a, the choice of cut-off between large and small particles that gives the flattest spectrum (solid black line) predicts spectral levels roughly 1 to 2 orders of magnitude larger than the observations, depending on the choice of concentration in the nearbed layer. However, this result is based on the assumption that all particles in the nearbed layer are involved in collisions at any instant in time (Equation 3.17). In reality, it is likely that only some fraction of particles in the nearbed layer is involved in the collision process at a given instant. If 5% of the total particles in the nearbed layer were assumed to be involved in collisions at any one time then the spectral levels of the predictions are brought in line with the observations (Figure 5.11b). The need to reduce the set of particles involved in collisions was also noted in previous lab work (*Thorne (1986)*) when predicting sound pressure levels from multiple collisions of particles in his rotating drum apparatus.

The relatively flat shapes of the measured spectra and the ability of the predicted spectra to produce a broad, relatively flat spectral shape (black line in Figure 5.11), at frequencies higher than 100 kHz, is further support for the hypothesis that SGN rigid body radiation is the mechanism of sound production. The predicted spectra exhibit decreased levels at frequencies below 100 kHz that is not reflected in the observations. This discrepancy at lower frequencies between predicted and observed spectra has also been noted in laboratory experiments (*Thorne* (1985,1986,2014)).

## **5.4 Discussion**

### **5.4.1 Less Intense Events**

The broadband noise associated with the arrival of quieter turbidity current fronts detected beneath the hydrophone (e.g. events D, F and G in Figure 5.2) is less intense and does not always arrive at roughly 10 s before the current front arrival, unlike the more intense events. However, due to the presence of appreciable sound energy at relatively high frequencies (> 200 kHz), it is likely that the sound source was near to the hydrophone, otherwise sound at these frequencies would have been severely attenuated by propagation through seawater. For these events, the noise presumed to be from the turbidity current arrives more than 10 s before the M3 detected front arrival, implying sound projected in the forward direction. The time difference is similar for events D and F but larger for event G. This can likely be explained by turbidity currents which were emitting sound up-channel of the hydrophone (in the down-channel direction), but had ceased by the time they were directly beneath, possibly due to a change in their dynamics.

As discussed in Section 5.2, the louder events focussed on in this work seemed to have a universal inability to project sound in the down-channel direction. This does not seem to be the case for the less intense events. Less intense events will likely have a lower sediment concentration driving them and may not be able to sufficiently agitate the bottom sediments enough to release bubbles. One or both of these factors may explain why weaker events seem to be able to project sound in the forward direction.

### **5.4.2 Bubble Generated Noise**

The shipboard single-beam sounders (Figure 4.1, and 4.2) clearly show evidence of bubbles being released by the passage of the turbidity current, and rising through the water column.

Bubbles are known sound producers in the ocean, and as such require thought in the context of this work. Evidence against bubbles being the source of the observed sound is seen in both the 28 kHz and 200 kHz single beam sonar data (Figure 4.1). The band of relatively short duration SGN (seen in Figure 4.1 and 4.2), which is not backscatter as explained previously, at roughly 16:49 is present only when the head of the current is in the vicinity of the instrument, whereas the bubbles, as seen from the backscatter, persist in the area for much longer. If the noise observed in the hydrophone record, associated with turbidity current events, was created by bubbles it would persist as long as the bubbles were in the vicinity of the instrument.

Further evidence against bubbles as the main sound producing mechanism can be seen in their size distribution, and the theory governing the relationship between bubble size and resonant frequency. As a first approximation bubbles as sound generators in the ocean are treated here as simple harmonic oscillators, in the first (breathing) mode. Equation 3.19 shows this resonant frequency (known as the Minnaert frequency) as a function of bubble size and pressure, and is plotted for the frequencies and depths appropriate to this work in Figure 5.12.

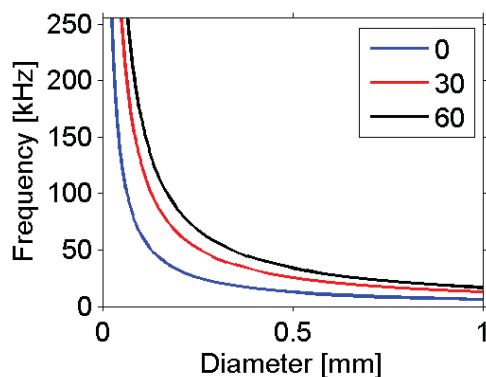


Figure 5.12: Minnaert resonance frequency as a function of diameter for three depths. The legend indicates water depth in m.

It is clear from the bubble size distribution (Figure 4.3) that very few are smaller than 0.2 mm, and the majority are in the vicinity of 1 mm. Bubbles in this size range therefore will have very little ability to create noise at frequencies above 100 kHz, as illustrated by Figure 5.12. Also, the bubble size distribution seems unlikely to be able to produce the

very flat spectra observed, even below 100 kHz. The distribution of bubble sizes (Figure 4.3), combined with the very peaked spectrum associated with bubble resonance (Leighton (2012)), would result in a more peaked spectrum, if bubble resonance were the main sound generation mechanism.

### 5.4.3 Remote Events and Frequency of Occurrence

Other interesting signals are sporadically observed in the hydrophone data. Examples of multiple such signals over an 8 min period on YD 172 (at roughly: 17:37, 17:39, 17:42 and 17:44) are shown in Figure 5.13.

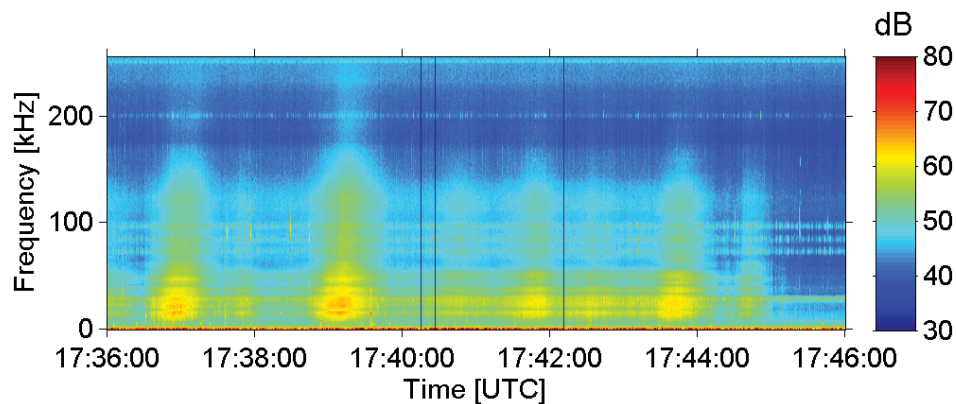


Figure 5.13: Ambient noise spectrogram for YD 172 showing signals suspected to be SGN from remotely occurring turbidity currents. Colours indicate dB re  $1 \mu\text{Pa}/(\text{Hz})^{1/2}$ .

These signals are attributed to turbidity currents in nearby channels on the delta face, the nearest of which was 400 m from the vessel location (Figure 5). This is because the fall-off in the higher frequencies of signal, from these potential remote currents, is qualitatively consistent with seawater sound absorption over a distance of roughly 400 m. As a basis for this conclusion, Figure 5.14 shows the effect of sea water absorption, over a 400 m distance, on the observed spectrum for event 172B: the reduced energy at high frequencies results in a spectrogram similar to those in Figure 5.13.

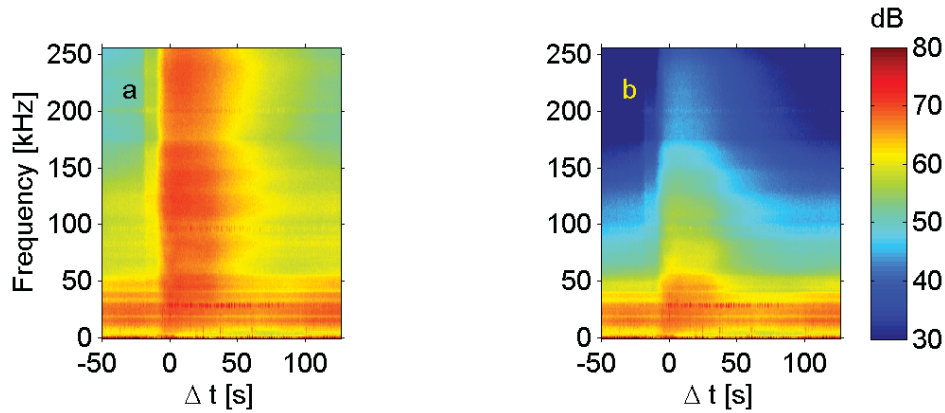


Figure 5.14: Spectrogram of turbidity current ambient noise signal: a) 10 m from source, and b) subjected to seawater absorption over a distance of 400 m. Colours indicate dB re  $1 \mu\text{Pa}/(\text{Hz})^{1/2}$ . Event 172B.

This evidence indicates that turbidity currents in this setting are detectable from remote channels, as well as the channel above which the hydrophone was deployed. Unlike those noise signals from currents flowing down the channel below the hydrophone, there is no temporal asymmetry in the signal presumed to be from these remote currents. This would be consistent with a source moving with constant speed towards, and then away, from the receiver, reaching some point of closest approach. This implies that the currents are able to project sound laterally.

Based on the assumption that the signals in Figure 5.13, and others like them, were from turbidity currents occurring remotely, the number of currents detected by the hydrophone was estimated. Qualitative identification of signals on YD 172 gave a total number of 44 events, 7 of which were independently detected by the M3 sonars directly beneath the hydrophone, and 2 of which were thought to travel very close to the hydrophone, due to the observed temporal asymmetry in their spectrograms and the flatness of their spectral shape. The record length for YD 172 was roughly 3.4 hr, which gives a frequency of occurrence of  $2.6 \text{ hr}^{-1}$  for events directly beneath the hydrophone, and  $12.9 \text{ hr}^{-1}$  for all events detected. Figure 2.1 shows what appear to be 4 main channels on the delta slope in which turbidity currents likely flow. If turbidity currents occurred at the same frequency in all channels as the channel directly beneath the hydrophone, a total frequency of occurrence of  $4 \times 2.6 = 10.6 \text{ hr}^{-1}$  would be expected.

#### 5.4.4 SGN: Comparing Predictions and Observations

Previous work (*Thorne (2014)*) has shown good agreement between predicted and observed spectral form for SGN. This work follows in that pattern. The broad, flat, observed spectra extending beyond 256 kHz are consistent with SGN being produced by particles of a broad size distribution, as measured at the field site. However, absolute spectral levels are not as easy to predict for SGN driven by a complex process, like a turbidity current. This work has shown a method by which predictions are made to match observations for spectral pressure levels, above 100 kHz, but it relies on many assumptions. Spectral levels are dependent on collision speed, number of collisions (in this case a function of choice of bedload concentration,  $C_{vbl}$ , among other things), whether collisions are head-on or glancing, the sizes of particles colliding, and the angle between the direction of the collision impact and the measurement position. Effort has been made in this work to justify the assumptions made in choosing these parameters, but spectral pressure levels are sensitive to all these somewhat uncertain assumptions and estimated parameters.

Regarding the discrepancy at lower frequencies between predicted and observed SGN spectra, it is possible that in these frequencies there are sources of sound related to the current from a mechanism of sound production other than SGN (e.g. bubbles). However, previous work (*Thorne (2014)*), has shown this discrepancy to exist even in a controlled setting where particle collisions were known to be the dominant sound source. This method assumes that the only collisions occurring are those between two individual particles isolated in the fluid. In reality, in a fluid of very high particle concentration such as the nearbed layer, collisions are likely frequently occurring between more than just two particles, either in the case of bunches of particles suspended or in particles colliding with the particles on the bottom. In both cases this may, in effect, increase the relative size of the colliding particle(s), potentially resulting in more sound energy in lower frequencies.

---

## CHAPTER 6

---

# SUMMARY AND CONCLUSIONS

Measurements of turbidity currents were made with multiple instruments during a field trip in Howe Sound in June 2013. This thesis focusses on using data from a broadband digital hydrophone to: (1) detect turbidity currents with passive acoustics; (2) determine the likely mechanism responsible for the sound produced by turbidity currents; and (3) establish a quantitative relationship between the properties of the flow, or associated bedload transport, and the intensity and frequency content of turbidity current noise.

*Turbidity Current Properties:* A total of 14 turbidity current events were observed to flow directly beneath the vessel and tethered instrument frame via the active sonar systems. For the 5 most intense events the M3 sonar data gave estimates of head speeds from 1.6 to 2.8 m/s, widths from 22 to 82 m, head heights from 1.1 to 4.6 m, and body thicknesses from 3.6 to 6.4 m. For event 172C, down-channel velocities from the ADCP data were found to peak at  $\simeq 2.5$  m/s and to decrease to  $\simeq 0.5$  m/s, roughly 0.5 to 7 min after the passage of the head. Suspended sediment concentration within the head of the current was estimated to be  $C_v \simeq 0.03$ , based on empirical formulae in the literature for head speeds on both flat and sloping bottoms. Suspended sediment concentration within the body was estimated at  $C_v \simeq 0.003$  assuming a force balance between the buoyancy force parallel to the bed, and the bottom friction. Independent estimates of  $C_v$  were obtained based on the differential attenuation of sound at two frequencies, and ranged from  $C_v \simeq 0.04$  in the head to  $C_v \simeq 0.005$  in the body.

*Observations of Turbidity Current Noise:* The shape of the noise spectra from these 5 events was relatively flat over the broad frequency range 20 - 256 kHz and exhibited no noticeable decrease up to the maximum frequency registered by the instrument (256

kHz). An abrupt increase in sound intensity preceded the arrival of the turbidity current front by roughly 10 s. This was determined to be due to an inherent inability of the most intense currents to project sound in the forward direction. The sound intensity peaked coincidentally with the arrival of the turbidity current front, and decreased gradually after the passage of the front, for a period of between roughly 2 to 13 min, depending on the event. For these 5 events a power law relationship between head speed and mean sound intensity levels (at 130-150 kHz) proportional to  $U_0^{7.1}$  was observed; however, the 90% confidence bounds of  $\pm 5.1$  on this value are broad.

*Turbidity Current Noise Modelling:* The balance of evidence suggests that the noise associated with these currents was predominately SGN. This motivated the prediction of a source sound spectrum based on the grainsize distribution, head speed of the current, and the analytical solution to the sound pressure field resulting from isolated, idealized collisions, detailed in *Thorne and Foden (1988)*. Following theory similar to that for collisions of molecules in the kinetic theory of gases, an equation was derived for particle collision rate per unit volume. This rate is proportional to the flow speed times the square of particle concentration, which in turn is proportional to flow speed squared: thus, collision rate is expected to be proportional to  $U_0^5$ . The theory for sound generated in a single collision indicates a dependence of acoustic intensity – i.e. sound pressure squared – on  $U_0^2$ . Thus, the theory indicates that the intensity of turbidity current noise is expected to be proportional to head speed to the power of 7, very close to the best-fit value of 7.1 indicated by the data.

The predicted SGN spectrum at the height of the hydrophone, 10 m, was calculated for conditions similar to event 172C, taking into account propagation effects through water, and the suspended sediment associated with the turbidity current. Sound-generating collisions were assumed to occur in the nearbed, high-concentration, coarser grain size layer, at constant speed  $U_c = 2u_*$ . The predicted spectral shape is primarily a function of the sizes of colliding particles, and is relatively flat above 100 kHz, similar to that observed, by excluding particles smaller than 0.8 mm. The predicted spectral levels, based on bottom layer concentrations of 10 to 20% by volume, are comparable to those observed, provided that only 5% of particles in the bedload layer are involved in collisions at any instant in time. At frequencies below 100 kHz, the predicted spectral levels were systematically lower than the observations. Both the results – i.e. the need to assume that only O(10%) of

the particles are involved in collisions, and the higher than predicted noise levels at low frequencies – are consistent with the results obtained by *Thorne* (1986) in his laboratory experiments with a particle tumbling apparatus.

Calculation of a theoretical effective listening radius for a single omni-directional receiver above a sound-emitting bottom with a layer of suspended sediment above it indicates that sound was unable to be projected out of the front of the more intense currents. Sound associated with the turbidity currents only became detectable when the current had entered the effective listening radius of the receiver. For some of the less intense events sound was observed that was likely projected out of the front of the turbidity current. Decreased sediment concentration in the head and/or the inability of the less intense currents to release bubbles from the bottom are speculated explanations for this effect.

*Distant Events:* Signals were observed in the hydrophone data that were attributed to distant events, supported by their spectral characteristics: i.e. a pronounced roll-off at high frequencies. These distant events were found to be qualitatively consistent with the 4 main channels experiencing turbidity currents at roughly the same occurrence frequency. Of the total events during the deployment detected by the hydrophone only 16% were independently detected by the other instruments. The occurrence frequency for the channel directly beneath the instrument frame was found to be  $2.6 \text{ hr}^{-1}$  and the total frequency of occurrence  $12.9 \text{ hr}^{-1}$  for the recording period on YD 172, so roughly 3 per hr for each of the 4 channels incising the delta front.

*Future Directions:* This work has shown passive acoustics to be a viable means for detecting turbidity current occurrence remotely, and could therefore provide the basis for a cost-effective long-term turbidity current monitoring system. The relationship between sound intensity and head speed suggests that – for the particular environment in which such a relationship has been established – not only the occurrence frequency, but also the head speed of the events can be inferred from ambient noise data. Hydrophone arrays, rather than single omnidirectional hydrophones, would provide important directional information on the sound from a turbidity current, as a function of position along its path.

## APPENDIX A

The pressure a sphere of radius  $a$  radiates undergoing a unit impulse acceleration  $P_i(t')$ , from Akay and Hodgson [1978] is given by:

$$P_i(t') = \frac{\rho_0 c a^2 \cos \theta}{r^2} e^{-\beta_2 l t'} \left[ \frac{1}{\beta_1} \left( 1 - \frac{\beta_2 r}{a} \right) \sin \beta_1 l t' + \frac{r}{a} \cos \beta_1 l t' \right] \quad (\text{A.1})$$

where  $\rho_0$  is the fluid density,  $c$  is the velocity of sound in the fluid,  $l = c/a$ ,  $r$  is the range from the sphere center, and  $\theta$  is the angle between the line of movement and the field position of measurement.  $\beta_1 = (1 - \beta)^{\frac{1}{2}}$  and  $\beta_2 = 1 + \beta$  with  $\beta = \rho_0/2\rho_s$ .

If two spheres collide, sphere  $i$  (radius  $a_i$ ) being stationary and sphere  $j$  (radius  $a_j$ ) travelling with velocity  $U_c$ , the hertzian acceleration time history of each sphere can be estimated as [Goldsmith 1960]:

$$A(t) = A_m (U_c \pi / 2 t_0) \sin(\pi t / t_0), \quad 0 \leq t \leq t_0 \quad (\text{A.2})$$

where

$$t_0 = 4.53 \left[ \left( \frac{1 - \sigma_i^2}{E_i \pi} + \frac{1 - \sigma_j^2}{E_j \pi} \right) \left( \frac{m_i m_j}{m_i + m_j} \right) \right]^{0.4} * \left( \frac{(a_i + a_j)}{U a_i a_j} \right)^{0.2} \quad (\text{A.3})$$

$t_0$  is the impact time duration,  $A_m U \pi / 2 t_0$  is the maximum acceleration of the sphere,  $m$  is mass,  $\sigma$  is Poisson's ratio and  $E$  is Young's modulus. A Hertzian collision framework implies: the strains are small and within the elastic limit, the surfaces are continuous and non-conforming, each body can be considered an elastic half-space, and the surfaces are frictionless. For each sphere  $A_m$  is:

$$A_{m_i} = 2m_j / (m_i + m_j), \quad A_{m_j} = -(m_i / m_j) A_{m_i} \quad (\text{A.4})$$

In a polar coordinate system with the origin at the point of contact of the two spheres, and the x-axis in-line with the centres of the spheres, let a receiver be at position  $(r, \theta)$ . The pressure the receiver sees is the sum of the pressures waves from each sphere, with a time delay for one pulse  $T_d$  due to the different path lengths to the receiver  $r_i$  and  $r_j$ . This time delay is approximated as:

$$T_d = \{[(a_i + a_j)(1 + \cos \theta) - 2a_j]/c\} + a_i(\pi/2 - 1)/c \quad (\text{A.5})$$

when  $\theta = 0$ . When  $\theta \neq 0$  the sphere radii are assumed equal and:

$$T_d = 2a \cos \theta / c \quad (\text{A.6})$$

otherwise.  $c$  is the speed of sound in the fluid.

With the acceleration time history and the impulse solution, the time convolution theorem can be used to obtain the power spectrum:

$$\begin{aligned} |P_P(f)|^2 = & P_0^2(f)[1 + \cos \pi f']/2(1 - f'^2)^2] * \{(R_1^2 + I_1^2) \\ & + (R_2^2 + I_2^2) + 2[(R_1 R_2 + I_1 I_2) \cos(\pi f' T_d / t_0) \\ & + (R_1 I_2 - R_2 I_1) \sin(\pi f' T_d / t_0)]\} \end{aligned} \quad (\text{A.7})$$

where  $P_0(f) = \rho_0 c U_c \cos \theta / r^2 \omega_0$ , with  $\rho_0$  being the density of the fluid.  $f' = f / f_0$ ,  $f_0 = 1/2t_0$ .  $R$  and  $I$  are the real and imaginary parts from the time convolution result, again with subscripts denoting for which sphere.

$$\begin{aligned} R = & a A_m(\{a \zeta [\zeta^2(\beta_1^2 + \beta_2^2) - f'^2] + 2r \zeta f'^2 \beta_2\} / \\ & [\zeta^4(\beta_1^2 + \beta_2^2)^2 + f'^4 + 2\zeta^2 f'^2(\beta_2^2 - \beta_1^2)]) \end{aligned} \quad (\text{A.8})$$

$$\begin{aligned} I = & a A_m(\{r f' [\zeta^2(\beta_1^2 + \beta_2^2) - f'^2] - 2a \zeta^2 f' \beta_2\} / \\ & [\zeta^4(\beta_1^2 + \beta_2^2)^2 + f'^4 + 2\zeta^2 f'^2(\beta_2^2 - \beta_1^2)]) \end{aligned} \quad (\text{A.9})$$

With  $\zeta = ct_0/\pi a$ ,  $\tau = t'/t_0$ ,  $t' = 1 - [(r - a)/c]$  and  $\rho_s$  is the density of the material making up the sphere.

---

## APPENDIX B

---

This thesis uses an empirical relationship by Brown and Lawler (2003) to calculate idealized spherical particle settling velocities and bubble rise rates. It is given by:

$$\hat{w}_s = \left[ \left( \frac{18}{\hat{d}^2} \right)^{((0.936\hat{d}+1)/(\hat{d}+1))0.898} + \left( \frac{0.317}{\hat{d}} \right)^{0.449} \right]^{-1.114} \quad (\text{B.1})$$

$\hat{w}_s$  and  $\hat{d}$  are dimensionless settling velocity and diameter given by:

$$\hat{w}_s = w_s \left[ \frac{\rho^2}{g\mu(\rho_s - \rho)} \right]^{\frac{1}{3}} \quad (\text{B.2})$$

$$\hat{d} = d \left[ \frac{g\rho(\rho_s - \rho)}{\mu^2} \right]^{\frac{1}{3}} \quad (\text{B.3})$$

where  $w_s$  is the terminal settling velocity and  $d$  is the particle diameter.  $\rho$  is the fluid density and  $\rho_s$  the particle density.  $g$  is the acceleration due to gravity and  $\mu$  is the absolute fluid viscosity.

Regarding bubble rise rates, this approximation falsely assumes bubble volume does not change as the bubbles rise through the water column, however, by approximating the bubbles rise rates as constant, it gives a measure of average bubble diameter over the measurement distance. In this work rise rates were estimated over a vertical distance of about 10 m, between depths 30 and 40 m.

# BIBLIOGRAPHY

- Akay, A., A review of impact noise, *The Journal of the Acoustical Society of America*, 64, 977–987, 1978.
- Akay, A., and T. Hodgson, Sound radiation from an accelerated or decelerated sphere, *The Journal of the Acoustical Society of America*, 63, 313–318, 1978a.
- Akay, A., and T. H. Hodgson, Acoustic radiation from the elastic impact of a sphere with a slab, *Applied Acoustics*, 11, 285–304, 1978b.
- Banerji, S., X. on aerial waves generated by impact. part ii, *The London, Edinburgh, and Dublin Philosophical Magazine and Journal of Science*, 35, 97–111, 1918.
- Banerji, S.-S., Vii. on aerial waves generated by impact, *The London, Edinburgh, and Dublin Philosophical Magazine and Journal of Science*, 32, 96–111, 1916.
- Barton, J. S., R. L. Slingerland, S. Pittman, and T. B. Gabrielson, Monitoring coarse bedload transport with passive acoustic instrumentation: A field study, *US Geol. Surv. Sci. Invest. Rep.*, 5091, 38–51, 2010.
- Bassett, C., J. Thomson, and B. Polagye, Sediment-generated noise and bed stress in a tidal channel, *Journal of Geophysical Research: Oceans*, 118, 2249–2265, 2013.
- Bedeus, K., and L. Ivicsics, Observation of the noise of bed load, *General Assembly, Commission on Hydrometry, International Association of Hydrological Sciences, Berkeley, CA, USA*, pp. 19–31, 1963.
- Bornhold, B. D., P. Ren, and D. B. Prior, High-frequency turbidity currents in british columbia fjords, *Geo-Marine Letters*, 14, 238–243, 1994.
- Britter, R., and P. Linden, The motion of the front of a gravity current travelling down an incline, *Journal of Fluid Mechanics*, 99, 531–543, 1980.
- Camenen, B., M. Jaballah, T. Geay, P. Belleudy, J. Laronne, and J. Laskowski, Tentative measurements of bedload transport in an energetic alpine gravel bed river, in *River flow*, pp. 379–386, 2012.
- Daly, R. A., Origin of submarine” canyons”, *Am. Jour. Sci.*, 31, 401–420, 1936.
- Ellison, T., and J. Turner, Turbulent entrainment in stratified flows, *Journal of Fluid Mechanics*, 6, 423–448, 1959.
- Fisher, F., and V. Simmons, Sound absorption in sea water, *The Journal of the Acoustical Society of America*, 62, 558–564, 1977.
- Fredsoe, J., R. Deigaard, and M. Stive, Mechanics of coastal sediment transport, *Journal of Fluid Mechanics*, 296, 408, 1995.

- Hay, A. E., Turbidity currents and submarine channel formation in rupert inlet, british columbia: 1. surge observations, *Journal of Geophysical Research: Oceans*, 92, 2875–2881, 1987.
- Heezen, B. C., and M. Ewing, Turbidity currents and submarine slumps, and the 1929 grand banks earthquake, *Am. J. Sci.*, 250, 849–873, 1952.
- Hughes Clarke, J. E., First wide-angle view of channelized turbidity currents links migrating cyclic steps to flow characteristics, *Nature communications*, 7, 2016.
- Hughes Clarke, J. E., S. Brucker, J. Muggah, I. Church, D. Cartwright, P. Kuus, T. Hamilton, D. Pratomo, and B. Eisan, The squamish prodelta: monitoring active landslides and turbidity currents, in *Canadian Hydrographic Conference 2012, Proceedings*, p. 15, 2012.
- Ingram, R., Sieve analysis, *Procedures in sedimentary petrology*, pp. 49–67, 1971.
- Johnson, M., Physical oceanography, *Science Progress (1933-)*, 50, 257–273, 1962.
- Johnson, P., and T. Muir, Acoustic detection of sediment movement, *Journal of Hydraulic Research*, 7, 519–540, 1969.
- Jonys, C., Acoustic measurement of sediment transport, *Scientific Series*, p. 64, 1976.
- Keulegan, G., An experimental study of the motion of saline water from locks into fresh water channels, *Nat. Bur. Stand. Rept. Technical Report*, 5168, 1957.
- Koss, L., Transient sound from colliding spheresnormalized results, *Journal of Sound and Vibration*, 36, 541–553, 1974a.
- Koss, L., Transient sound from colliding spheresinelastic collisions, *Journal of Sound and Vibration*, 36, 555–562, 1974b.
- Koss, L., and R. Alfredson, Transient sound radiated by spheres undergoing an elastic collision, *Journal of Sound and Vibration*, 27, 591N169–681N275, 1973.
- Leighton, T., *The Acoustic Bubble*, Elsevier Science, 2012.
- Mason, T., D. Priestley, and D. Reeve, Monitoring near-shore shingle transport under waves using a passive acoustic technique, *The Journal of the Acoustical Society of America*, 122, 737–746, 2007.
- McNaught, A. D., and A. Wilkinson (Eds.), *IUPAC. Compendium of Chemical Terminology, 2nd ed. (the "Gold Book")*, vol. 1669, Blackwell Scientific Publications, 1997.
- Nielsen, P., *Coastal bottom boundary layers and sediment transport*, vol. 4, World Scientific Publishing Co Inc, 1992.
- Plapp, J. E., and J. P. Mitchell, A hydrodynamic theory of turbidity currents, *Journal of Geophysical Research*, 65, 983–992, 1960.

- Porter, M. B., The bellhop manual and users guide: Preliminary draft, *Heat, Light, and Sound Research, Inc., La Jolla, CA, USA, Tech. Rep*, 2011.
- Porter, M. B., and Y.-C. Liu, Finite-element ray tracing, *Theoretical and computational acoustics*, 2, 947–956, 1994.
- Prior, D. B., B. D. Bornhold, W. J. Wiseman Jr, and D. R. Lowe, Turbidity current activity in a british columbia fjord, *Science*, 237, 1330–1334, 1987.
- Richards, K., and L. Milne, Problems in the calibration of an acoustic device for the observation of bedload transport, *Earth Surface Processes*, 4, 335–346, 1979.
- Sequeiros, O. E., H. Naruse, N. Endo, M. H. Garcia, and G. Parker, Experimental study on self-accelerating turbidity currents, *Journal of Geophysical Research: Oceans*, 114, 2009.
- Serway, R., *Physics for Scientists & Engineers*, Physics for Scientists & Engineers, Saunders College Pub., 1990.
- Simpson, J. E., *Gravity currents: In the environment and the laboratory*, Cambridge university press, 1997.
- Stacey, M. W., and A. J. Bowen, The vertical structure of density and turbidity currents: theory and observations, *Journal of Geophysical Research: Oceans*, 93, 3528–3542, 1988.
- Thorne, P., An overview of underwater sound generated by interparticle collisions and its application to the measurements of coarse sediment bedload transport, *Earth Surface Dynamics*, 2, 531, 2014.
- Thorne, P. D., The measurement of acoustic noise generated by moving artificial sediments, *The Journal of the Acoustical Society of America*, 78, 1013–1023, 1985.
- Thorne, P. D., Laboratory and marine measurements on the acoustic detection of sediment transport, *The Journal of the Acoustical Society of America*, 80, 899–910, 1986.
- Thorne, P. D., and D. J. Foden, Generation of underwater sound by colliding spheres, *The Journal of the Acoustical Society of America*, 84, 2144–2152, 1988.
- Thorne, P. D., A. D. Heathershaw, and L. Troiano, Acoustic detection of seabed gravel movement in turbulent tidal currents, *Marine geology*, 54, M43–M48, 1984.
- Topping, D., S. Wright, T. Melis, and D. Rubin, High-resolution measurements of suspended-sediment concentration and grain size in the colorado river in grand canyon using a multi-frequency acoustic system, in *Proceedings of the 10th International Symposium on River Sedimentation*, vol. 3, p. 19, 2007.
- Tywniuk, N., and R. Warnock, Acoustic detection of bed-load transport, in *Hydrology Symposium, Department of Environment: Natural Resource Council, University of Alberta, Edmonton, Alberta*, pp. 8–9, 1973.

- Urick, R., The absorption of sound in suspensions of irregular particles, *The Journal of the acoustical society of America*, 20, 283–289, 1948.
- Voulgaris, G., M. P. Wilkin, and M. B. Collins, The in situ passive acoustic measurement of shingle movement under waves and currents: instrument (tosca) development and preliminary results, *Continental Shelf Research*, 15, 1195–1211, 1995.
- Williams, J. J., P. D. Thorne, and A. D. Heathershaw, Comparisons between acoustic measurements and predictions of the bedload transport of marine gravels, *Sedimentology*, 36, 973–979, 1989.
- Xu, J., M. Noble, and L. K. Rosenfeld, In-situ measurements of velocity structure within turbidity currents, *Geophysical Research Letters*, 31, 2004.
- Zeng, J., D. R. Lowe, D. B. Prior, W. J. Wiseman, and B. D. Bornhold, Flow properties of turbidity currents in bute inlet, british columbia, *Sedimentology*, 38, 975–996, 1991.